International Journal of Fatigue 32 (2010) 1473–1502

Contents lists available at ScienceDirect

International Journal of Fatigue

journal homepage: www.elsevier.com/locate/ijfatigue

Nanostructurally small cracks (NSC): A review on atomistic modeling of fatigue

M.F. Horstemeyer [a,*], D. Farkas [b], S. Kim [a], T. Tang [a], G. Potirniche [c]

[a] Center for Advanced Vehicular Systems, Mississippi State University, Mississippi State, MS 39762, USA
[b] Department of Materials Science and Engineering, Virginia Polytechnic Institute and State University, Blacksburg, VA 24061, USA
[c] Department of Mechanical Engineering, University of Idaho, Moscow, ID, USA

ARTICLE INFO

Article history:
Received 8 June 2009
Received in revised form 4 January 2010
Accepted 15 January 2010
Available online 1 February 2010

Keywords:
Embedded atom method
Fatigue
Nanostructurally small crack
Atomistic modeling
Structural nanomaterials

ABSTRACT

Fatigue is one of the most damaging mechanisms in structural components. With the development of structural nanomaterials, it is imperative to investigate the fatigue damage phenomena at the atomic scale. To study fatigue behavior at the nanoscale, one must apply non-continuum modeling frameworks, such as molecular statics (MS), molecular dynamics (MD), and Monte Carlo (MC) methods. To date, only MD and MS simulations using embedded atom method (EAM) and modified embedded atom method (MEAM) potentials have been conducted, and this paper reviews these simulations of the nanoscale fatigue-crack growth in nickel and copper including single crystals, bicrystals, and polycrystals. A nanoscale size middle tension (MT) specimen with the lateral side applied periodic boundary conditions was used to investigate the fatigue behavior in nickel and copper single crystals. Simulation results revealed that the cyclic plastic deformation at the crack tip was the main influencing factor for fatigue-crack growth. Two main nanoscale mechanisms of crack propagation were observed: (1) the main cracks linked with the voids nucleated in front of crack tip due to high dislocation density generated by the cyclic loading; and (2) the main cracks broke the atomic bonds in the crack plane without much plasticity. For the bicrystals and polycrystals, the grain boundaries exerted resistance to the crack propagation. To study the interactions between cracks and grain boundaries, four cases of grain boundary interfaces for copper and two cases of grain boundaries for nickel were simulated. In copper bicrystals, the crack path deviated and moved from one grain to another for high misorientations, while there were voids nucleating at grain boundaries in front of the crack tip that linked back with the main crack. Similar to macroscale fatigue, dislocation substructures were observed to develop in the atomic lattice during cyclic loading. In nickel bicrystals, for large misorientations, the cracks were stopped by grain boundaries. For small misorientations, the crack propagated through the grain boundary, but the growth rate was reduced due to the resistance of the grain boundary. Fatigue-crack growth rates for nanocracks were computed and compared with growth rates published in the literature for microstructurally small cracks (micron range) and long cracks (millimeter range). A nanostructurally small crack (NSC) was introduced in terms of the CTOD. The quantified NSC growth rates in copper single crystals were very similar with those experimentally measured for small cracks (micron range) and with those at stress-intensity-factor ranges lower than the threshold for long cracks (millimeter range). The atomistic simulations indicated that reversible plastic slip along the active crystallographic directions at the crack tip was responsible for advancing the crack during applied cycling. In the case of single or double plastic slip localization at the crack tip, a typical Mode I fatigue crack arose along a slip band and then grew into a mixed Mode I + II crack growth mechanism. For crystal orientations characterized by multiple slip systems concomitantly active at the crack tip, the crack advance mechanism was characterized by nanovoid nucleation in the high density nucleation region ahead of the crack tip and by linkage with the main crack leading to crack extension. To facilitate observations of fatigue-crack growth, the simulation of a copper polycrystal was performed at low temperature 20 K as well. The crack propagated along persistent slip bands within the grain. The crack propagated along grain boundaries when the angle between the direction of crack propagation and the grain boundary was small, while it was impeded by the grain boundary when the angle was large. The results obtained for the crack advance as a function of stress intensity amplitude are consistent with experimental studies and a Paris law exponent of approximately two.

* Corresponding author.
E-mail addresses: mfhorst@cavs.msstate.edu, mfhorst@me.msstate.edu (M.F. Horstemeyer).

0142-1123/$ - see front matter © 2010 Elsevier Ltd. All rights reserved.
doi:10.1016/j.ijfatigue.2010.01.006

1. Introduction

Fatigue in metallic materials subject to repeated cyclic loading has been an active research area since last century and continues to be a focus of structural materials study. Most investigations of fatigue have been performed at the microscale and/or macroscale. Hence, the mechanism of fatigue failure is fairly well understood with the crack lengths ranging from a few microns to millimeters/centimeters. The classic continuum approaches are very powerful tool to solve the problems at the macro- or microscale. However, several reasons exist for performing atomic scale simulations. First, due to the development of nanomaterials and nanostructures, fatigue will become, at some point, an issue for the designers. Without the knowledge base for nanoscale fatigue, the designs will not be as robust. Second, macroscale fatigue models, particularly ones with microstructural sensitivities do not cover the length scale in the atomic region. To garner nanoscale crack growth rules in order to get more accurate macroscale predictive tools, atomistic simulations are warranted to provide mechanism understanding of grain boundary effects, crystal orientation effects, and driving force versus material resistance effects. Finally, nanoscale fatigue simulations such as those provided in this review can give insight into the fidelity of higher scale mathematical models and micromechanical finite element simulations by either providing the pertinent equations or at least the parameters for already developed equations.

With respect to multiscale fatigue models, several have recently been developed [1–5] precious few have focused on the nanoscale. Since atomistic modeling is a useful tool to help understand and model the motion of each atom in the material, molecular dynamics and statics simulations can provide understanding into the dislocation nucleation, motion, and interaction with cracks. As opposed to continuum theories, atomistic modeling is capable of providing insight into solving fatigue problems based more on first principles. As long as the interatomic potential is reliable, it can disclose the fundamental physical mechanisms of fatigue. As such, some questions that have driven the research in atomistic fatigue are the following: can the equations that represent the microstructurally small crack growth regimes be used for nanocrack growth since material resistance is present at both length scales? Can long crack growth models be used to capture the nanocrack growth rates? Does the crystallographic orientation effect change our paradigm of small crack growth? Do we see the same mechanisms at the nanoscale as we do at the microscale and macroscale?

To provide context for the nanoscale fatigue study presented here, it is worth mentioning that extensive studies on single crystal, bicrystal, and polycrystalline under monotonic loads have been accomplished by several researchers. Daw et al. [49] provided a nice summary of using embedded atom method (EAM) potentials for understanding dislocation nucleation and propagation, application to hydrogen environments, and issues with free surfaces like cracks. Holian et al. [81] and Abraham et al. [82] were probably the first to examine large scale parallel computing simulations of cracks growing via molecular dynamics simulations. Baskes et al., [57] studied biomaterials interfaces under monotonic loads. Gall et al. [58] conducted molecular dynamics simulations to study the crack growth of aluminum–silicon biomaterial interfaces. Fang et al. [59] performed Bauchinger effect studies by examining single and bicrystal nickel specimens to associate the type of dislocations with reverse yielding effects. Clearly, a whole review is warranted just to discuss the plasticity and fracture related to atomistic simulations, but a few seminal papers were mentioned here to provide context for the nanoscale fatigue discussions ahead.

The fatigue behavior of materials has not been studied extensively at atomic level. The basic reason is relate to the difficulties arising from the associated length and time scales. To the best of our knowledge, only several researchers conducted the computational study on fatigue-crack growth of face-centered cubic metal, namely, copper and nickel at atomic scale [6–9]. The results of atomistic simulation by Farkas et al. [9] are consistent with the experimental results of fracture and fatigue in a bulk nanocrystalline Ni–Fe alloy carried out by Yang et al. [10] who revealed that the fatigue crack in the nc Ni–Fe alloy initiated by nanovoid coalescence ahead of the dominant crack tip. Nishimura and Miyazaki [11] performed the molecular dynamics simulation of α-Fe to examine the mechanical behaviors around a crack tip for a system containing both a crack and two tilt grain boundaries under cyclic loading. They proposed that the fatigue-crack growth mechanism is due to the coalescence of the crack and the vacancies caused by the emission and absorption of the dislocations at the crack tip. Chang and Fang [12] analyzed the tensile and fatigue behavior of nanoscale copper at various temperature using molecular dynamics simulation. They concluded that the effect of increasing temperature is an increase in fatigue stress and the ductile fracture configuration occurred under lower applied stress.

In light of the aforementioned comments, the focus of this paper is to present a review on the atomistic modeling of fatigue-crack growth in single crystals, bicrystals, and polycrystals of copper and nickel reported in [6–9]. We try to sum up the works performed in this field so far. The survey of the literature is included in Sections 2–4. We also added some new atomistic fatigue-crack growth results in nickel bicrystals and copper polycrystals, which had not been published in the literature. The summary is presented in the final section with thoughts regarding new areas of research regarding atomistic modeling of fatigue.

2. Simulation method

2.1. Interatomic potentials

In atomistic modeling, the properties of materials can be defined by the interatomic potential (to a continuum mechanics person, this is the constitutive relationship), which is the basic input of molecular simulation besides the structural information such as the initial configuration of atoms, type of atoms and their velocities, etc. The choice of interatomic potential is vital to the simulation results. The embedded atom method (EAM) potential was devised to solve practical problems in metals with many-body bonding properties [13,14] and were used the fatigue studies of [6–9]. EAM treats each individual atom as an embedded particle in a host aggregate composed of all the other atoms. The embedding energy contributes to the total energy of the system through the local electron density where an individual atom is located. The EAM theory is based on local-density functional principles and its central idea is that the cohesive energy of a system can be described as the energy provided by an atomic system during the embedding process of each constituent atom in that particular system, as given in the equation

$$E = \sum_i G_i\left(\sum_{j\neq i}\rho_j^a(R_{ij})\right) + 1/2\sum_{i,j(i\neq j)}U_{ij}(R_{ij}) \tag{1}$$

where G is the embedding energy, ρ^a is the average electron density, R_{ij} is the distance between the atoms i and j and U is the energy due to the electrostatic interaction between two atoms [14]. As shown Eq. (1), an important assumption is that the embedding energy of any atom (which can be viewed as an impurity) is a function of the electron density of the host before the atom is added. The functions G_i and U_{ij} are calculated from experimental curve fitting of the lattice parameter, elastic constants, and sublimation and vacancy formation energies [13]. An improvement to the EAM is the modified embedded atom method (MEAM) potential [15,16]. In

the MEAM, the electron density is given by two terms, the linear superposition of the electron densities from the neighbouring atoms and a correction term that takes into account the angularity of the atomic bonds correlated to the shear modulus [16]. The specific form of the atom density function in the MEAM [15] is given by

$$\rho_i^a = \sum_{j\neq i} \rho^a(R_{ij}) - a \sum_{j\neq i, k\neq i} (1 - 3\cos^2 \theta_{jik} \rho^a(R_{ij}\rho^a(R_{ik}))) \quad (2)$$

where R_{ij} is the distance between atoms i and j, a is the angularity parameter calculated by correlation with the shear modulus and θ_{jik} is the angle between the atoms i, j and k. The form in Eq. (2) was chosen to minimize the distortional energy. The MEAM was shown by [15] to work well for metals and for other types of materials (semiconductors and diatomic gases).

In this paper, MEAM potential was used to simulate the fatigue-crack growth in copper and nickel single crystals and copper bicrystals. The EAM potential was applied to simulate the fatigue-crack growth in nickel bicrystals and copper nanocrystalline materials. The simulations utilize an EAM potential for nanocrystalline Ni [17] and has been tested as part of our previous work dealing with fracture under monotonic loading [18].

Also, if one were to use molecular dynamics to perform fatigue cycling on polymers and/or ceramics, one would probably not need to use EAM or MEAM potentials. A good summary of the class of bond order formalisms that has proven valuable for covalently bonded systems was given by Brenner [54]. Stoneham et al. [55] summarized the shell model, which is a modification of a pair potential, used for ceramics.

2.2. Atomistic model set-up

2.2.1. Single crystals

To simulate the fatigue-crack growth in copper and nickel single crystals, five specimens with different orientations were employed to study the nanoscale fatigue-crack growth in copper and nickel single crystals. These orientations, shown in Fig. 1, are [1 1 1], [1 0 0], [1 1 0], [1 0 1] and [1 2 2], respectively. These orientations represented the crystallographic directions corresponding to the y-axis of the specimen along with the loading that was applied. The x-axis represented the crack growth direction, whereas z represented the thickness dimension of each specimen. Five orientations of the specimens were chosen for the analysis, since they constitute representative directions on the stereographic triangle or the inverse pole figure. In addition, each of these orientations were characterized by a varying number of slip systems initially active as shown in Table 1. The atomistic models for each of the five orientations were built with approximate dimensions of $36 \times 36 \times 1.4$ nm, in the x-, y- and z-directions, respectively. The thickness of the model in z-direction is four times of the unit cell length depending on the indices of z-axis after [50,51]. In order

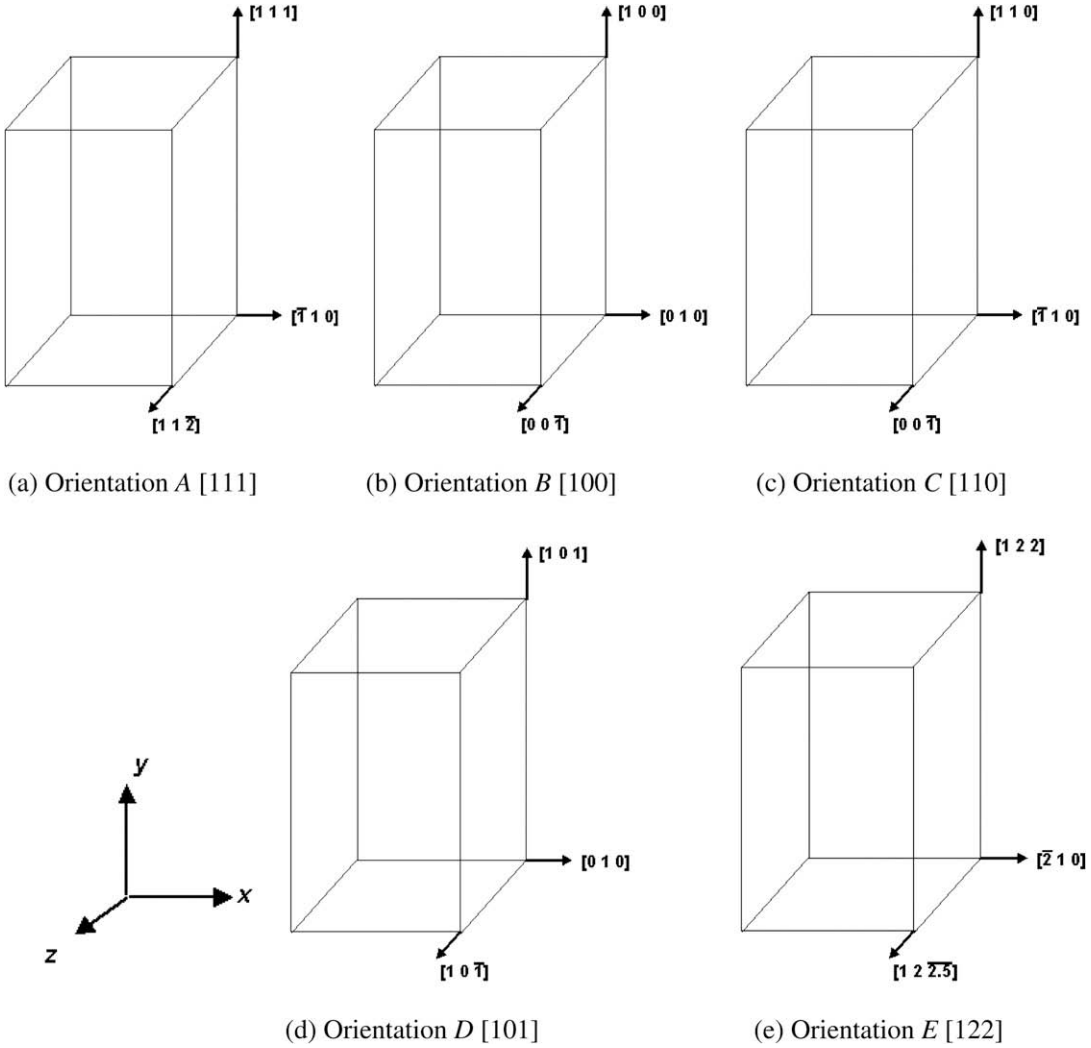

(a) Orientation A [111] (b) Orientation B [100] (c) Orientation C [110]

(d) Orientation D [101] (e) Orientation E [122]

Fig. 1. Lattice orientation analyzed in the single crystal simulations.

Table 1
Summary of fatigue-crack growth data in single crystals.

Orientation	No. of active slip systems	Schmid factor	Propagation mode	Crack extension mechanism
A [1 1 1]	6	0.272	Mode I	Ductile
B [1 0 0]	8	0.408	Mode I	Ductile
C [1 1 0]	4	0.408	Mode I	Cleavage
D [1 0 1]	4	0.408	Mode I + II	Ductile
E [1 2 2]	2	0.408	Mode I + II	Ductile

to verify the effects of z-direction thickness and potential, we have also performed the simulation on the models with the thickness in z-direction having eight and twelve times of one unit cell length using the potential given by Mendelev et al. [19]. The simulation results show that the results have converged when there are four unit cell in z -direction and the results obtained using Mendelev potential have the same trends as those calculated by MEAM [15].

Another nuance related to the boundary conditions is related to the periodic boundary conditions. Once a dislocation would initiate within the specimen, it might cut through the specimen and come through the other side looking like a new dislocation. It is, however, just the same one because of the limitation of the periodicity. This phenomena was observed in several other studies where large strain plasticity was studied as well [52,53]. Although one could assert that each of the boundaries could act as a grain boundary, where dislocations would nucleate accordingly, it is still a nuance of the boundary conditions employed. One could imagine that other types of boundary conditions would induce different dislocation behavior and thus affect the specimen behavior. Some who have studied these effects include the following: this is an opportunity for future studies.

Therefore, in the following investigations, we employ the MEAM [15] to investigate the fatigue-crack growth in copper and nickel single crystals. The periodic boundary conditions were assigned in the x- and z-directions. Each specimen had an initial central crack (middle tension configuration). The atomistic specimens were assigned periodic boundary conditions in the x- and z-directions. Each specimen included an initial central crack (middle tension configuration).

The ratio of the initial crack length to the width of the specimen was $a_0/W = 0.1$. Cyclic loading was applied at a strain rate of $10^9\ s^{-1}$. Also, an initial velocity gradient was employed throughout the specimen so as to remove the shock moving through the specimen as per [52].

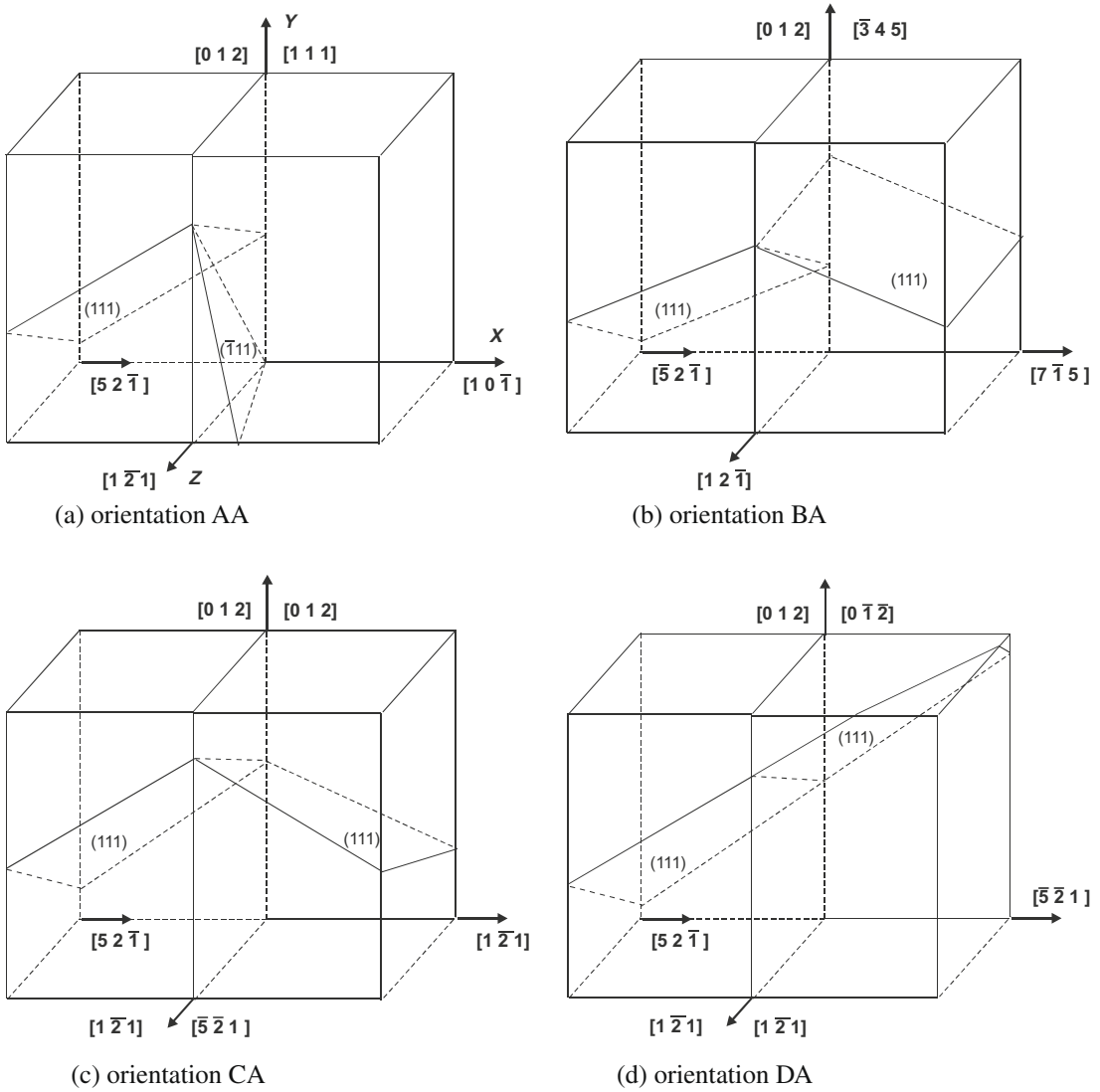

Fig. 2. Lattice orientations for the two grains in the bicrystal simulations.

2.2.2. Bicrystals

In the bicrystals studied in this work, the notion of small misorientation angles and large misorientation angles were analyzed after the large strain work of Hansen and Hughes [56]. Clearly, more important grain boundaries or ones that are maybe more prevalent in copper and nickel should be studied, but this present study only examines some idealizations to show the connections to higher scale models. Work has been conducted at the atomic scale for bicrystals [70–75] and polycrystals [76–80] by examining types of dislocations and plasticity but mainly upon monotonic loading conditions [65–69].

2.2.2.1. Copper bicrystals. Four cases of grain boundary interfaces were simulated in the study of fatigue-crack growth in copper bicrystals. The general configurations of these bicrystals follow the types experimentally analyzed by Li [20], and they are shown in Fig. 2. The first case AA, shown in Fig. 2a, corresponds to a [0 1 2]–[1 1 1] tilt grain boundary. The *z*-axis corresponds to the [1 $\overline{2}$ 1] direction for both neighbouring grains, while the *x*-axis in the first grain is represented by the [5 $\overline{2}$ 1] direction, and in the second grain by the direction. The second case BA corresponds to a [0 1 2]–[$\overline{3}$ 4 5] tilt grain boundary and is shown in Fig. 2b. The primary slip directions [1 0 1](1 1 1) in the two adjacent grains are symmetrical with respect to the vertical grain boundary, forming a 101.3° angle between them. Fig. 2b shows that the primary slip planes in the two grains are not parallel to each other. The third case CA corresponds to the two grains being oriented in a [0 1 2] tilt symmetric orientation related to the tensile *y*-axis. The orientation of the *x* and *z* axes for each of the grains are shown in Fig. 2c. The two primary slip systems intersect the grain boundary plane along a common axis, and their components in the *x*-direction are inversely related to each other. The fourth case DA is a [1 $\overline{2}$ 1] tilt boundary shown in Fig. 2d. The tensile axis is represented in the first grain by [0 $\overline{1}$, $\overline{2}$] direction and in the second grain by [0 1 2]. The primary slip planes (1 1 1) in the two grains are parallel to each other. In each of these cases, the grain on the left had an edge crack. The fatigue loading applied to the specimens was similar to the loading conditions applied to the single crystal specimens and has been described in the previous section.

2.2.2.2. Nickel bicrystals. The bicrystals of nickel comprised two symmetrically rotated single crystals, as shown in Fig. 3, which are demarcated by a tilt grain boundary. The orientation of the [1 1 0] axes of the two single crystals were inclined by equal angles to the [0 0 1] axis. The angle between the [1 1 0] axes of two single crystals was defined as θ. The size of the specimen was

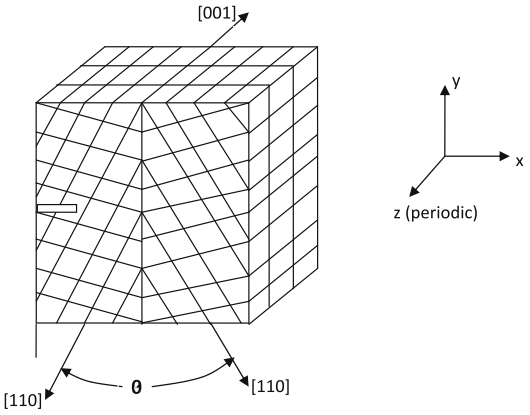

Fig. 3. Orientation of bicrystal [1 1 0] axes of the two symmetrical single crystals are inclined by equal angles to the [0 0 1] axis.

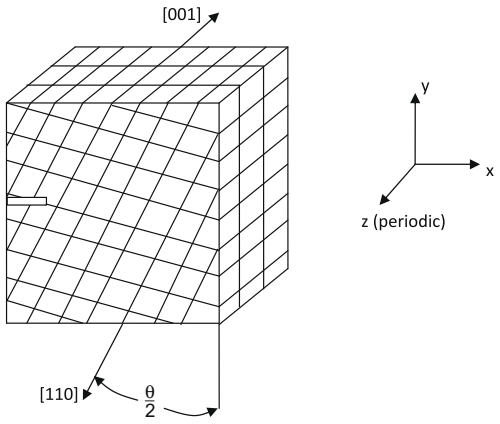

Fig. 4. Orientation of the corresponding single crystal.

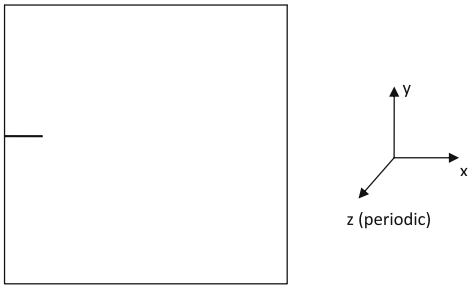

Fig. 5. Specimen used for the simulation of fatigue-crack growth.

42.4 × 28.2 × 1.4 nm, in the *x*-, *y*-, and *z*-directions, respectively. We investigated two cases of grain boundary, namely, $a\theta = 10°$ small misorientation and $a\theta = 30°$ large misorientation grain boundary. There was an edge crack on the left edge of each specimen. For the sake of comparison, we also simulated the fatigue-crack growth in corresponding single crystal as shown in Fig. 4, whose dimensions were the same as those of bicrystals.

The applied cyclic loading was $\varepsilon_{max} = 5 \times 10^{-2}$ and stress ratio $R = \varepsilon_{min}/\varepsilon_{max} = 0.8$ for the bicrystal nickel simulations. The loading was applied along *y*-direction, and the periodic boundary condition was assigned in *z*-direction.

2.2.3. Nanocrystalline FCC metals

2.2.3.1. Copper nanopolycrystalline. Voronoi construction was employed to build the initial atomic configuration [21]. All of the columnar grains in the specimens were constructed using the common axis [0 0 1] around which each grain rotated random angles. We made three specimens containing 5, 20, and 40 grains, respectively. After the initial generation, the specimens were equilibrated at a temperature of 20 K. To facilitate the propagation of fatigue crack, the simulation was performed at 20 K also. Each specimen had an initial edge crack on the left as shown in Fig. 5. The dimensions of each specimen are 16 × 16 × 1.4 nm. The increasing maximum strain fatigue loading as shown in Fig. 29 was applied along the *y*-direction.

2.2.3.2. Nickel nanopolycrystalline. Just like the copper polycrystalline specimens, the initial nickel atomic configurations used in our studies were generated using a Voronoi construction [21] as well. The columnar grains in the sample were generated by using a common [1 1 0] axis for all grains and a random rotation angle around this axis for the various grains. The sample contained 36

grains with an average grain size of 6 nm. The periodicity along the [1 1 0] axis common to all grains was kept at the lattice periodicity along that direction. The grain boundaries present in these samples were of pure tilt character and had random misorientation angles. After their initial creation, the samples were fully relaxed using a conjugate gradient technique. The initial relaxation included the simultaneous energy minimization with respect to the total sample volume. The relaxed configuration was then used as a starting configuration in both the molecular statics and the dynamics techniques to study crack propagation using the same EAM interatomic potential and cyclic loading.

The simulation of fracture in nickel was conducted differently than in the copper nanocrystalline specimens. With the notion of a semi-infinite crack loaded to a given stress intensity K, the molecular dynamics and molecular statics simulations employed displacement fields obtained from the elasticity theory for the given value of the stress intensity. The role of the linear elastic continuum displacement served as an initial guess for the relaxed atomic configuration in all the regions of the simulation. It also served as the boundary conditions that were kept fixed in the regions far from the crack tip. Based on continuum fracture mechanics, the elastic solution should be valid far from the crack tip. The atomic positions far from the crack tip were held fixed according to the elastic solution during the conjugate gradient routine used in molecular statics or during a certain number of time steps in the molecular dynamics technique. As the simulation progressed, the loading increased or decreased superposing corresponding displacement given by linear elasticity, updating the fixed boundary conditions to those representatives of a crack with a higher or a lower loading level. These displacements were used to simulate cyclic loading by applying a load to a certain stress intensity K_{max} for the first part of the cycle and then superposing displacements corresponding to reach a lower stress intensity K_{min} in the second part of the cycle. The cyclic process between the maximum and minimum stress intensities can be simulated with either molecular dynamics or molecular statics. The latter technique simulates an equilibrium configuration in the crack tip at both the minimum and maximum loading points of each cycle. Alternatively, molecular dynamics represents the response of the crack tip at extremely high cycling rates. In the work reported here we used both techniques.

The samples were subject to cyclic loading with an average stress intensity, K_{ave} of 0.96 MPa $\sqrt{m}$. Four values of the stress intensity amplitude were considered, namely, 1.28, 1.6, 1.76, and 2.9 MPa $\sqrt{m}$. For the molecular dynamics simulations 2000 MD steps per cycle were used with a time step of 1×10^{-15} s and a temperature of 300 K. Simulations using molecular statics were also carried out where the crack was allowed to reach a local equilibrium configuration at both the low and the high loading points of the cycle. These simulations were therefore representative of low cycle fatigue where the system has enough time to reach equilibrium as the cycle proceeds. Most importantly, the comparison of these two techniques gave an assessment of the importance of the fast time scale in the MD simulations in the mechanisms observed and in the rates of crack advance. The simulations reported here follow the crack using this technique for 30 cycles. The threshold stress intensity amplitude observed was about 1–1.1 MPa $\sqrt{m}$.

2.3. Discussion of effects of boundary conditions

The major difficulty with the nanofatigue simulations is the strong constraint imposed by using periodic boundary conditions in the z-direction with a relatively small through-thickness dimension. Some have studied these effects based upon monotonic loads [62–64]. As mentioned earlier, this can give quantitative differences in the results although the qualitative trends would not be affected as discussed in [50–53]. In these nanofatigue simulations, different crystal orientations have a geometry in which the [1 1 1] slip planes did not contain the out-of-plane line direction and so are oblique to the crack front. This suppresses dislocation emission on the accepted slip planes arising in FCC materials. Therefore, such complex dislocation behavior in three dimensions remains as a need for future study.

To verify the effect of thickness in z-direction, we performed the investigations on the specimen with Orientation C as shown in Fig. 1c. The thickness varied from four unit cell to twenty unit cells. The length of one unit cell was about 0.35 nm, and a uniaxial tension strain in the y-direction was applied up to a total strain of $\varepsilon = 0.06$. The averaged stress–strain curves of the different thickness specimens are shown in Fig. 19. We observed that the stress dropped once the dislocations nucleated at the crack tips. The initial slope of the stress–strain curve and dislocation nucleation stress were independent of the thickness in the z-direction. This implies that the first dislocation nucleation was not affected by the specimen thickness. Also, the cyclic loading was applied along the y-direction. Fig. 20 shows the crack growth rate decreased abruptly when the thickness increased from four unit cells to eight unit cells. The results converged at the thickness of 16 unit cells.

2.4. Visualization

We use the centrosymmetry parameter defined by Kelchner et al. [22] to highlight the dislocations in the specimen for the most part. This parameter for each atom is given by

$$P = \sum_i |R_i + R_{i+6}|^2 \tag{3}$$

where R_i and $R_i + 6$ are the vectors corresponding to the six pairs of nearest opposite neighbors in the FCC lattice. Thus, $P = 0$ in an undisturbed portion of the lattice, and P becomes large near dislocations or free surfaces. The centrosymmetry parameter is a metric introduced to quantify nanoscale defects. For example, a vacancy represents a situation where only individual atoms are displaced from their original equilibrium position, while the surrounding lattice remains intact. A dislocation in the atomistic model represents a continuous line of atoms with modified centrosymmetry parameters.

Another parameter that we employed for visualization purposes was the Green strain tensor adapted from Gullett et al. [60]. The different components of the strain tensor were employed to give insight into the centrosymmetry parameter results and also provide fodder for the local plastic shear strain range used in McDowell et al. [61].

3. Simulation results

3.1. Fatigue-crack growth in single crystals

3.1.1. Copper single crystals

The loading applied was in a strain-controlled mode with the maximum strain level of $\varepsilon_{min} = 0.01$ and an applied load ratio of $R = \varepsilon_{min}/\varepsilon_{max}$. This high load ratio for the tension–tension fatigue loading was chosen to prevent the crack faces from contacting each other, otherwise partial rewelding of the crack faces occurred, leading to difficulty in growing the crack. All atom velocities were initiated in the required direction at the beginning of each loading and unloading half cycle to alleviate the stress wave overlap that could arise from the high rate of deformation. Before applying the fatigue loading, the temperature in the specimens was equilibrated at 300 K. During fatigue loading for the first 10–15 cycles, we did not observe the mean stress relaxation. However, for most

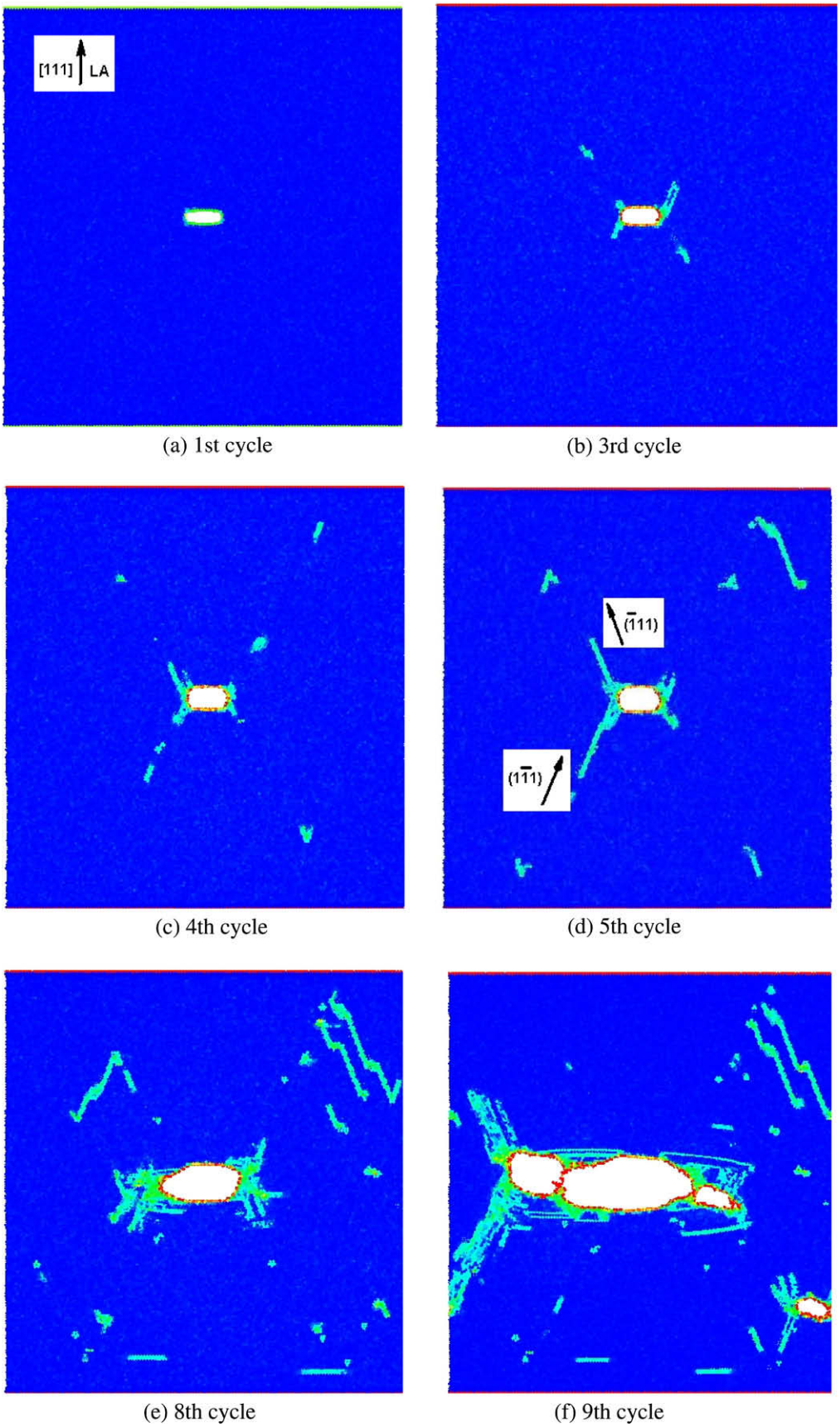

Fig. 6. Contour plots of plastic deformation and crack growth during fatigue loading for a single crystal in Orientation A [1 1 1] coincident with the loading axis (LA).

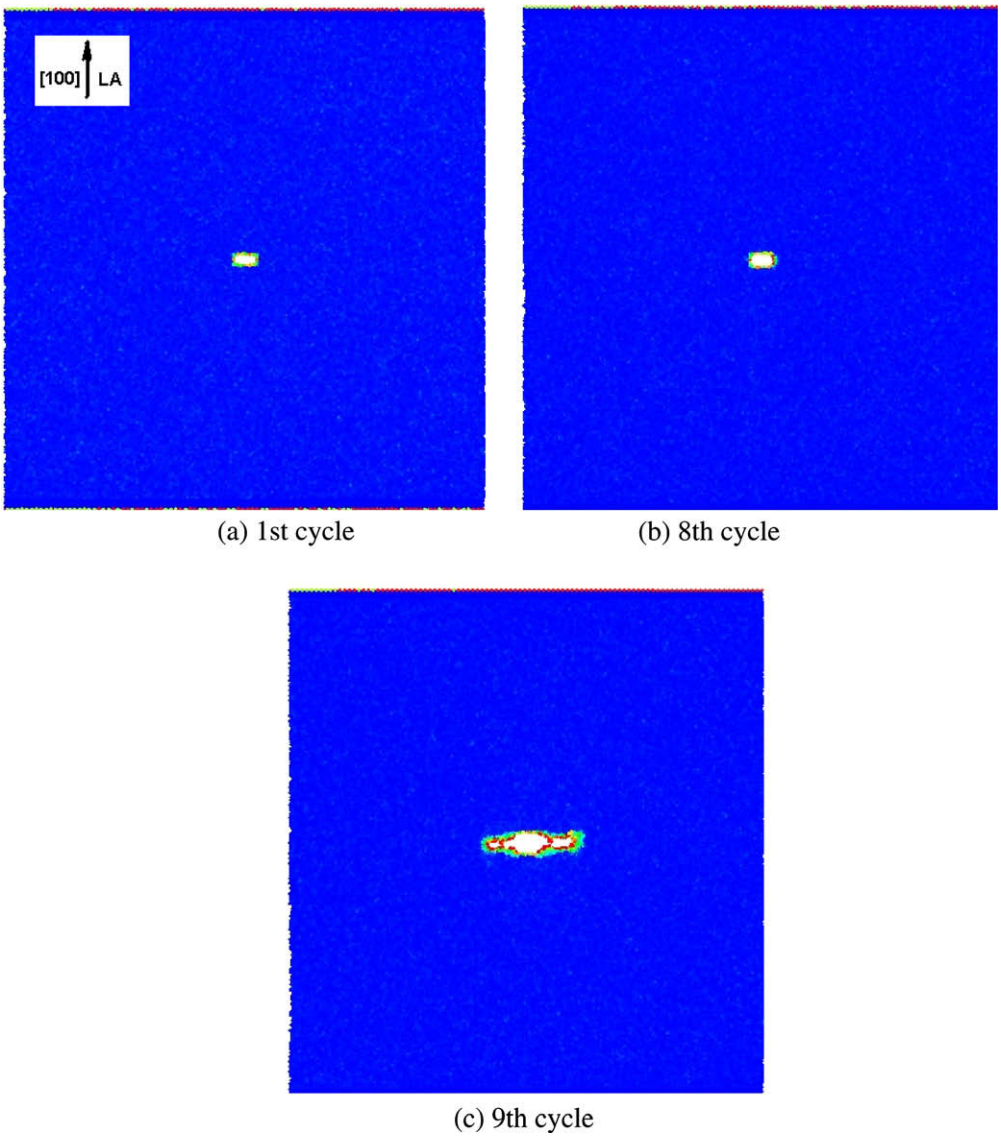

Fig. 7. Contour plots of plastic deformation and crack growth during fatigue loading for a single crystal in Orientation B [1 0 0].

crystal orientations analyzed, the mean stress stabilization was recorded.

The mechanisms of fatigue crack propagation at the macroscale for long cracks and at the microscale for small cracks have been studied intensely [23–25]. These cracks grow as Stage II fatigue cracks at rates up to several microns per cycle. Nanoscale cracks exhibit growth rates in the vicinity of several angstroms per cycle. Using atomistic simulations, insight into the crack propagation mechanisms at the smallest length scales governed by plastic deformation can be gained. In this section, we show that the plastic processes leading to crack propagation at the nanoscale operate similarly as in the case of small and long cracks.

Figs. 6–10 show fatigue-crack growth in the specimens indicated in Fig. 1a–e. These figures show contour plots of the plastic deformation around the crack tip at various loading cycles for all five orientations considered. In the case of Orientation A, shown in Fig. 6, the crack grew in the plane (1 1 1), propagating along the $[\bar{1}\,1\,0]$ direction, and the view plane is $(1\,1\,\bar{2})$. The two slip bands forming at the crack tip correspond to the directions [1 3 2] and [3 1 2], representing the traces the slip planes $(1\,\bar{1}\,1)$ and $(\bar{1}\,1\,1)$, respectively on the view plane $(1\,1\,\bar{2})$. The slip bands were oriented at an angle of 22.2° with respect to the vertical [1 1 1] orientation. The crack tip exhibited significant blunting due to the intense localization of the plastic slip along the two slip bands. An increased dislocation density in front of the crack tip caused void nucleation and linkup of the voids with the main crack leading to a crack growth increment. Fig. 3 shows the simulation results from Orientation B. The crack plane was (1 0 0) and propagation occurred along [0 1 0] direction. The crack tip plastic zone was small and localized near the crack tip. Consequently, the crack tip blunting was relatively small, according to the reduced plasticity at the crack tip. The propagation mechanism in this case was void nucleation in front of the crack tip and linkage of the void back to the main crack. Since eight slip systems were concomitantly active at the crack tip, plasticity at the crack tip similar to an isotropic condition produced high stress triaxialities (Fig. 7).

Fig. 8 shows results from Orientation C with the crack in the (1 1 0) plane and the propagation direction along $[\bar{1}\,1\,0]$. No significant crack tip blunting was observed in this case. Multiple slip orientations induced a crack propagation mechanism characterized by fatigue cleavage of atoms in the (1 1 0) plane.

Fig. 9 shows Orientation D of the atomistic model with the crack in the (1 0 1) plane and propagating in the [0 1 0] direction. Intense double slip localization occurred at the crack tip. The two slip

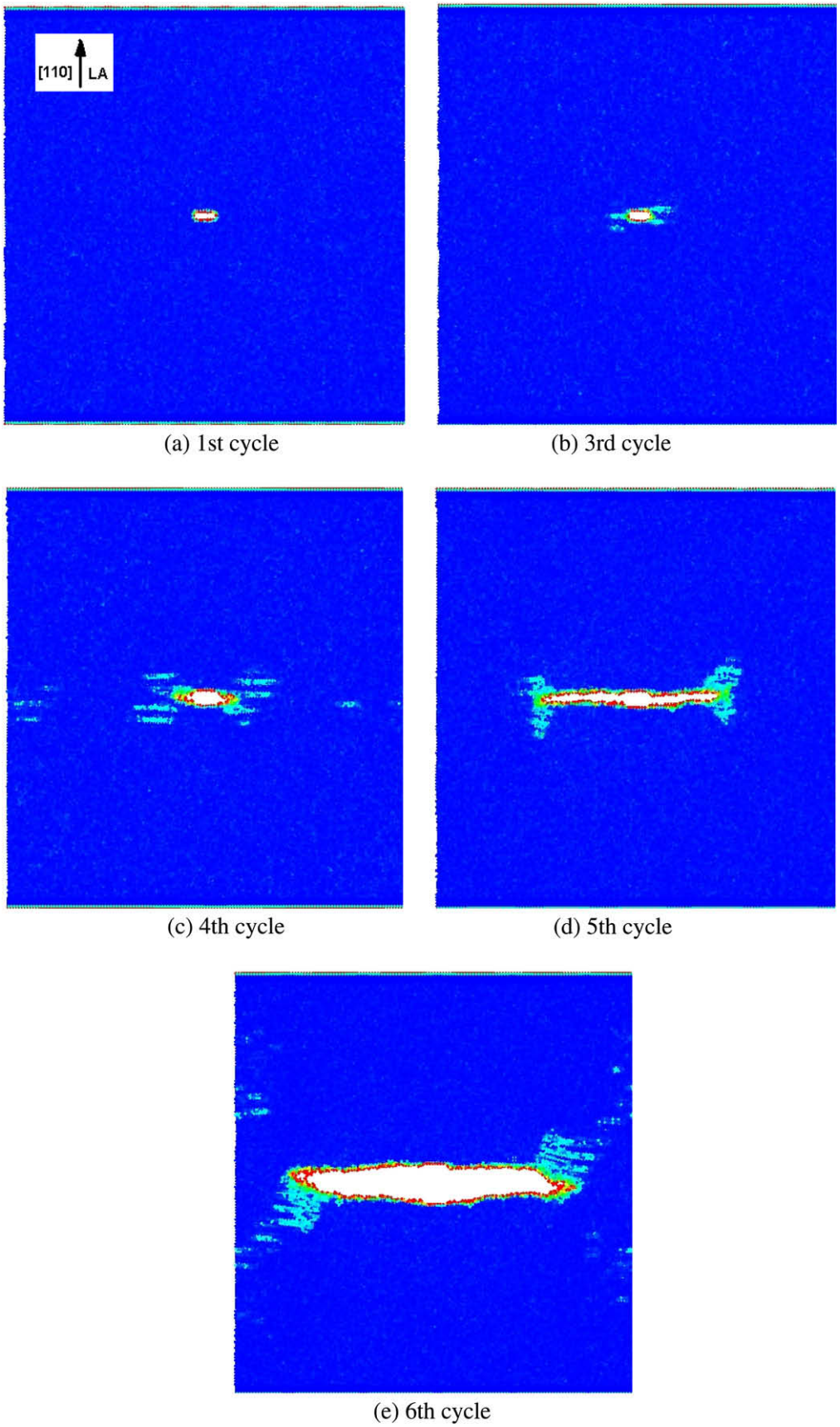

Fig. 8. Contour plots of plastic deformation and crack growth during fatigue loading for a single crystal in Orientation C [1 1 0].

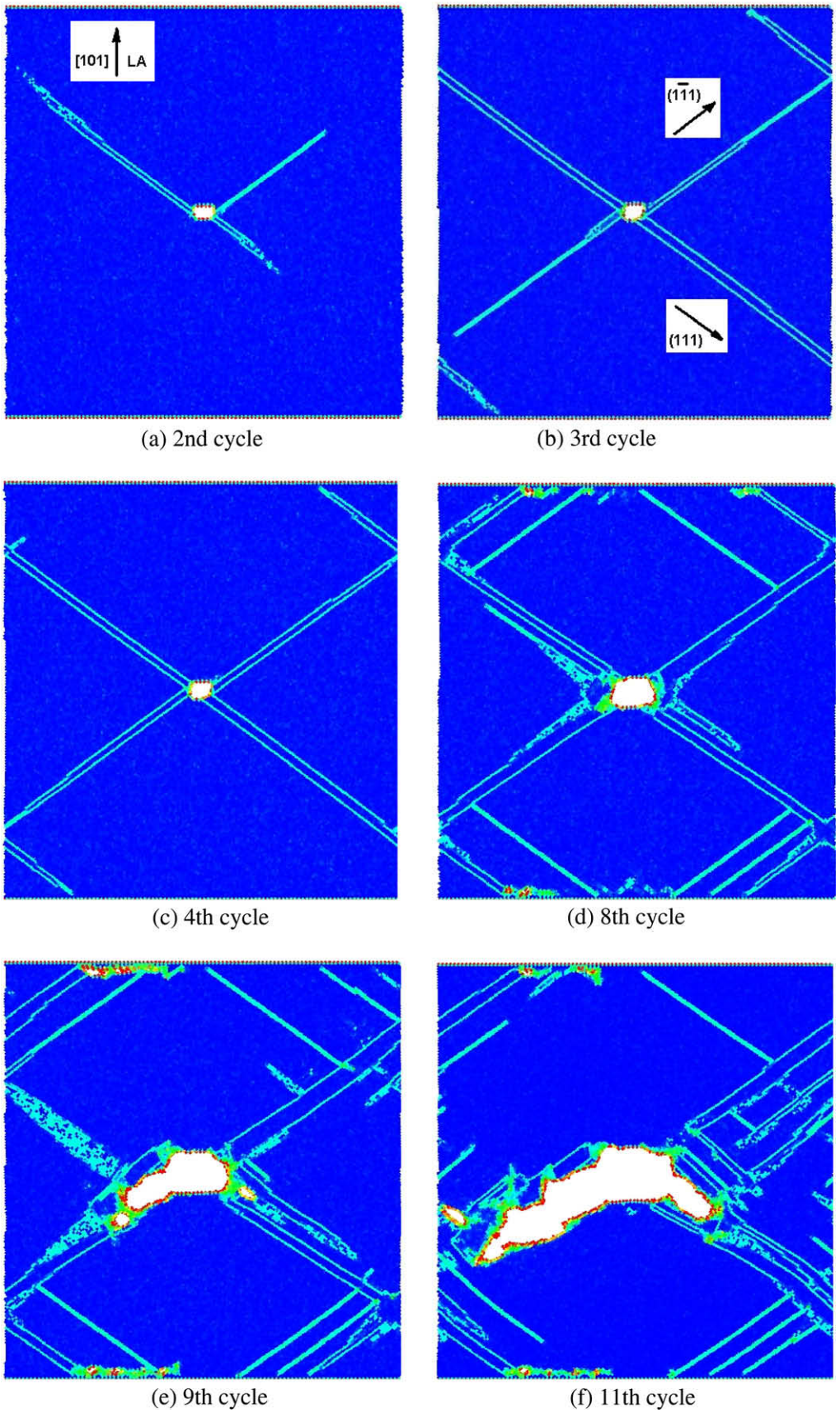

Fig. 9. Contour plots of plastic deformation and crack growth during fatigue loading for a single crystal in Orientation D [1 0 1].

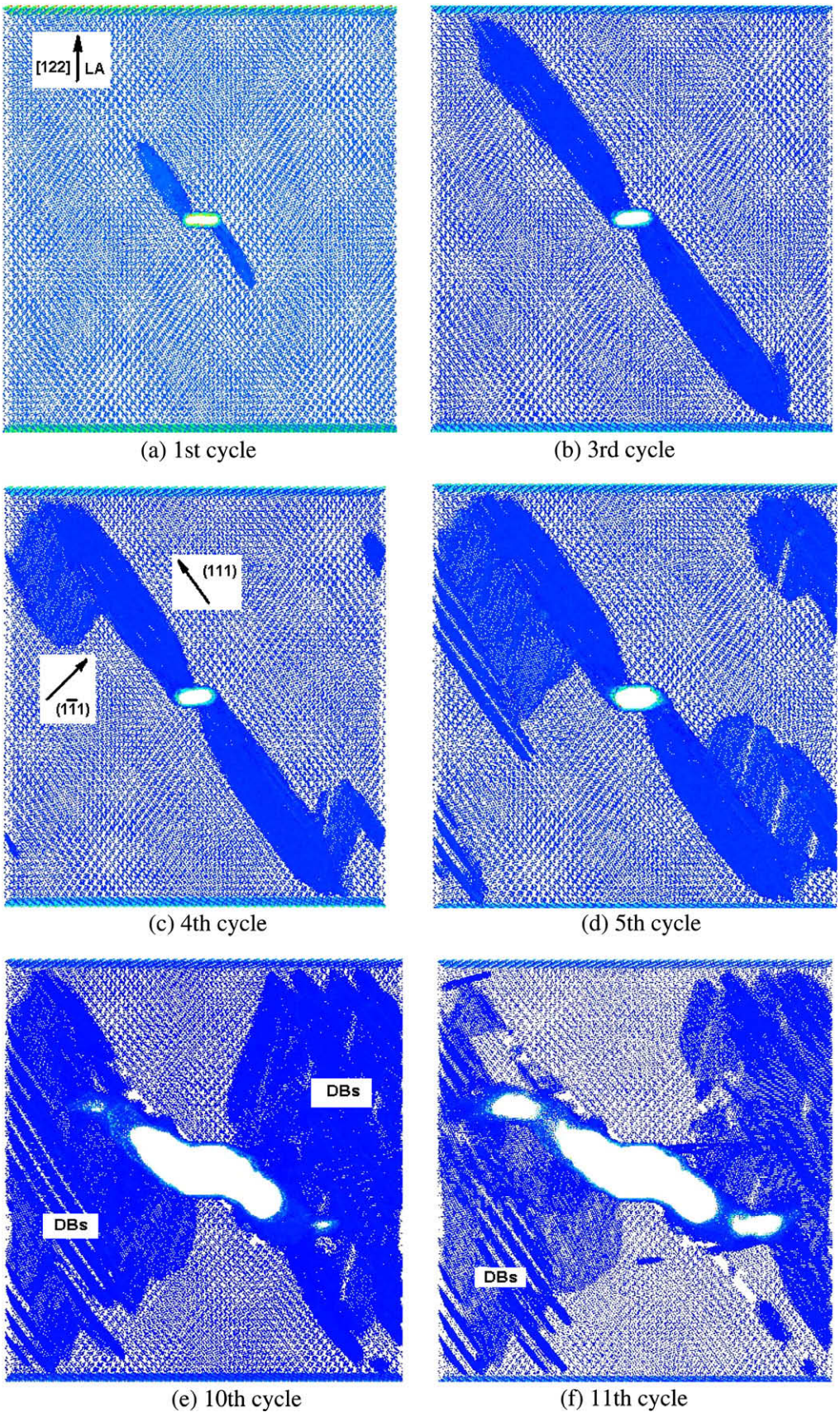

Fig. 10. Contour plots of plastic deformation and crack growth during fatigue loading for a single crystal in Orientation E [1 2 2].

bands corresponded to the directions [1 2 1] and [1 $\bar{2}$ 1], representing the intersections of the view plane (1 0 $\bar{1}$) with the slip planes (1 $\bar{1}$ 1) and (1 1 1), respectively. Significant crack tip blunting was experienced by the crack due to the plastic slip localization at 54.7° with respect to the vertical [1 0 1] direction. Between Cycle 2 and Cycle 8, the crack grew under Mode I. Starting at Cycle 9, the crack deviated out-of-plane into mixed Mode I + II of growth along the primary slip bands. Growth along a crystallographic slip bands has also been observed for larger microstructurally small cracks within crystallographic grains [26]. The results from Orientation E shown in Fig. 10 had a crack located in the (1 2 2) plane and growing in the [$\bar{2}$ 1 0] direction. A single slip band formed at the crack tip along the primary slip direction [9 7 1], which is the trace of the (1 1 1) slip plane with the view plane (1 2 $\overline{2.5}$). Plastic shear occurred along the secondary slip system in the [1 7 6] direction, which is the intersection between the (1 $\bar{1}$ 1) slip plane and the view plane. The angle between the slip line [9 7 1] and the vertical axis [1 2 2] was geometrically calculated to be 43.2°. Crack tip blunting occurred similar to Orientation D as shown in Fig. 1d. Also, similar deviation of the crack was observed, from a Mode I growth to a mixed Mode I + II growth along the primary slip band. Deformation bands (DBs) are observed to cover a wide area of the specimen with even distribution of dislocations, as opposed to the slip bands where the majority of plastic deformation is limited to a narrow band. Usually DBs are highly deformable regions extending over a large portion of the specimen surface, and they dominate the cyclic deformation in FCC single crystals [27,28]. A summary of the main findings from the fatigue-crack growth simulations in single crystals is shown in Table 1.

To compare the various nanoscale crystal orientation effects, fatigue-crack growth rates were computed from the atomistic simulations for two strain levels of $\varepsilon_{max} = 0.02$ and 0.01. Figs. 11 and 12 show the crack growth rates da/dN versus the stress-intensity-factor range ΔK. The Mode I stress-intensity-factor range has been calculated using

$$\Delta K = K_{max} - K_{min} \quad \text{and} \quad K = \sigma\sqrt{\pi a} \tag{4}$$

where σ is the volume average stress in the y-direction calculated from the dipole force tensor of all atoms in the model, and a is the crack length. The value of the geometrical factor multiplying the right-hand side of Eq. (4) was calculated and based upon the different atomistic results were not larger than 1.02. Thus, for simplicity, in Eq. (4), we assumed this factor to approximate one. Crack growth rates da/dN versus ΔK for an applied strain of $\varepsilon_{max} = 0.02$ are shown in Fig. 11 The results from this study are compared with experimental data for microstructural long cracks from the literature. This comparison gives a multiscale view of the fatigue-crack growth phenomenon in copper. A few important comments are warranted. First, nanocracks exhibit growth rates that are comparable to those of fatigue cracks from the higher length scales. However, the computed da/dN for nanocracks range between 10^{-11} and 10^{-8} m/cycle, while long cracks were found to grow at rates lower than 10^{-11} m/cycle in the experiments of Marchand et al. [29] in the near-threshold regime, for copper with two grain sizes of 12 and 120 μm, respectively. In polycrystalline copper, Liaw et al. [30] recorded da/dN for copper at two heat-treatment conditions ranging from approximately 10^{-10} to values larger than 10^{-7} m/cycle. The crack growth rates computed from our atomistic simulations were slightly lower than the growth rates experimentally measured in copper single crystals oriented for single slip by Wang and Mughrabi [31], who found da/dN ranging from 5×10^{-9} to 2×10^{-8} m/cycle. Growth rates for microstructurally small cracks were measured by Pol'ak and Li¢skutin [32], and they indicated a classical small crack effect growing faster than long cracks in single crystals and long cracks.

Crack growth rates from atomistic simulations with a maximum applied $\varepsilon_{max} = 0.01$ are shown in Fig. 12 with those of microcracks and long cracks in single and polycrystals. For the convenience of comparison of the values obtained from $\varepsilon_{max} = 0.01$ and $\varepsilon_{max} = 0.02$, we also plotted the atomistic simulation results from $\varepsilon_{max} = 0.02$ in the Fig. 12. The crack growth rates for $\varepsilon_{max} = 0.01$ were comparable with those for $\varepsilon_{max} = 0.02$. From Figs. 11 and 12 one can observe that, besides the comparable da/dN, the crack tip driving force ΔK values for cracks at different length scales were amazingly in the same range. In Fig. 11, the ΔK values computed for nanocracks ranged from 0.3 to 1.2 MPa $\sqrt{m}$. These values for ΔK were well below the threshold value ΔKth for long cracks in copper polycrystals experimentally measured at approximately 2 MPa $\sqrt{m}$ [32]. For an applied maximum strain of $\varepsilon_{max} = 0.01$ the crack tip driving force decreased to approximately 0.05 MPa $\sqrt{m}$. Below this value, the nanoscale cracks in the present study were observed to become non-propagating, suggesting a threshold between propagating and non-propagating

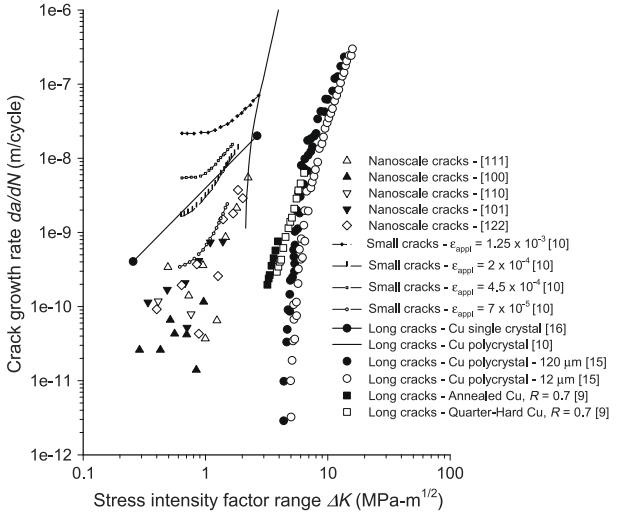

Fig. 11. Crack growth rates from the nanoscale atomistic simulations comparing small and long crack growth rates in Cu single and polycrystals. The applied maximum strain was $\varepsilon_{max} = 0.02$.

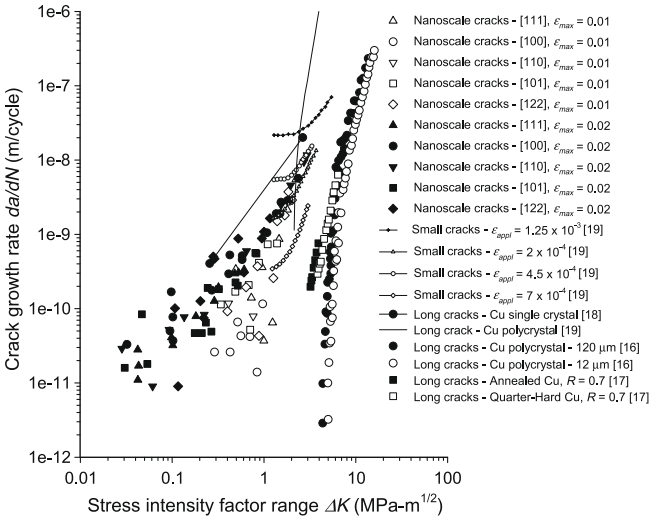

Fig. 12. Crack growth rates from the nanoscale atomistic simulations comparing small and long crack growth rates in Cu single and polycrystals. The applied maximum strain was $\varepsilon_{max} = 0.01$ and 0.02.

fatigue cracks at the nanoscale between 0.05 and 2 MPa $\sqrt{m}$. However, a more systematic study, using at least one of the well-known methods (constant K_{max} or constant R) will be required for a rigorous characterization of ΔKth for nanocracks.

The growth rates for nanocracks computed from atomistic simulations indicated that as the applied ΔK was lowered toward a value of approximately 0.05 MPa $\sqrt{m}$, the scatter in growth data increased considerably. On the contrary, for larger ΔK values, the crack growth rates do not exhibit significant scatter, and the data tends to be positioned on a well-defined line on the da/dN versus ΔK plot. This suggests the existence of a Paris [33] regime for nanocracks. For the computations with the applied maximum strain level of $\varepsilon_{max} = 0.02$, the Paris equation obtained by curve fitting the crack growth data for $\Delta K \geqslant 1.06$ MPa $\sqrt{m}$ is

$$\frac{da}{dN} = C(\Delta K)^m \tag{5}$$

where, C and m are constants with $C = 3.149 \times 10^{-10}$ and $m = 3.504$. Similar curve fitting for the data in Fig. 12, for $\varepsilon_{max} = 0.01$, resulted in $C = 2.387$ and $m = 9.05 \times 10^{-10}$.

Based on the results obtained from the atomistic simulations and comparison with fatigue-crack growth data shown in Figs. 11 and 12, a map of crack growth rate distributions for cracks ranging from the nanoscale to macroscale can be drawn. In Fig. 13, such a map is shown, indicating distinct regions for growth rates of fatigue cracks of various lengths. At the smallest length scale, with nanocrack lengths ranging between 1 nm and 1 μm, the crack growth rates da/dN can vary from approximately 10^{-11} to 5×10^{-10} m/cycle depending on the crystal orientation, for an applied stress intensity range, ΔK, from a threshold value of approximately 0.05 to 2 MPa $\sqrt{m}$, respectively. In this regime, nanocracks grow under the influence of discrete dislocations and atomic motion, such as plastic slip localization along crystallographic planes and vacancy formation. The next level in material length scale is represented by microstructural cracks with lengths ranging from 1 μm to approximately 1 mm. Fatigue-crack growth mechanisms are influenced mainly by the microstructural features encountered by the fatigue crack during its growth history. Among these, the most important are grain boundaries [34], inclusions, and constituent particles [35]. The region on da/dN versus ΔK plot for microstructural cracks is above the one for nanocracks. Based on experimental results [32], microstructural cracks in copper have a growth rate between 5×10^{-10} and approximately 2×10^{-8} m/cycle for the same applied values of ΔK. The largest length scale

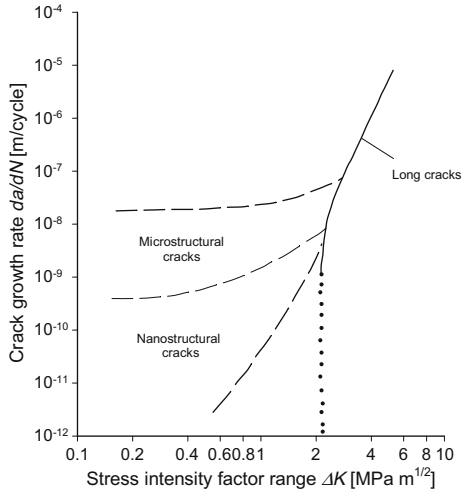

Fig. 13. Crack growth rate map for fatigue cracks ranging from nanoscale to macroscale in copper single and poly-crystals.

for fatigue cracks is represented by long cracks, larger than 1 mm. For this type of crack, the only governing mechanism is the plastic deformation in the wake and at the crack tip. The growth of long cracks is observed usually for ΔK values larger than approximately 2 MPa $\sqrt{m}$. As ΔK is increased, the crack growth of a long crack can be represented by a Paris Law type Eq. (5).

Traditionally, for long cracks, researchers have considered that the crack growth increment during a cycle is a fraction of the crack tip opening displacement (ΔCTOD) range. This is supported by the reversible crack tip blunting processes [23]. However, in the case of small cracks, a breakdown of the linear elastic fracture mechanics principle occurs [24,25]. The growth rates of small cracks can be much larger than those for long cracks, which makes the increment in growth rate sometimes equal to ΔCTOD. In the case of fatigue nanocracks, such a topic has not been studied either experimentally or computationally. Correlation of the crack growth rate da/dN versus the ΔCTOD for nanocracks is shown in Fig. 6. The CTOD was measured at a very short distance behind the crack, usually between 1 and 2 nm, where the crack tip blunting ended and the crack faces became flat. At any position, the dependence of da/dN versus ΔCTOD is represented by

$$\frac{da}{dN} = c\Delta\text{CTOD} \tag{6}$$

where c is a constant determined from atomistic computations. The constant c is observed to vary from one orientation to another. For example, the constant c has a low value of 0.38 in the case of orientation [1 0 0], while it has similar values of 1.25 and 1.52 for orientations [1 1 1] and [1 0 1], respectively. The simulations in the case of orientation [1 2 2] required a large value of 2.16 for the constant c. In addition, values greater than one for the constant c for some orientations imply that the fatigue damage progressed rapidly at the nanoscale. An explanation for this situation is that, in the case of nanocracks, the crack length a, crack growth increment da/dN, and opening displacement range ΔCTOD are all of comparable dimensions, in the range of nanometers. On the contrary, at the microscale, da/dN is approximately two to three orders of magnitude smaller than a (Fig. 14).

3.1.2. Nickel single crystals

Dislocation substructures that arose during the cyclic loading at constant strain amplitude were analyzed, and the main results are presented in Figs. 15 and 16. The fatigue loading applied had a maximum strain of $\varepsilon_{max} = 5 \times 10^{-3}$ and a ratio of $R = \varepsilon_{min}/\varepsilon_{max} = 0.5$. The high load ratio was chosen in order to prevent the inner faces of the void from contacting each other during unloading. From previous simulations, it was observed that contact of the crack surfaces led to the welding of the crack faces which led to difficulty in propagating the crack. All the specimens were cyclically loaded up to 11 cycles at which point the simulations were stopped. Fig. 15 presents the dislocation structures observed during the cyclic loading. These patterns varied widely from one orientation to another. In the case of Orientation A [1 1 1] crystallographic direction, the nickel single crystal experienced a triple slip pattern with the three main shear bands nucleating from the small circular void. One of the shear bands aligned with the x-direction, corresponding to the $[\bar{1}\,1\,0]$ direction, while the other two shear bands were positioned symmetrically about the [1 1 1] direction (y-axis). In the case of Orientation B, with the loading in the [1 0 0] direction, practically very little plastic deformation was experienced by the single crystal, and the slip was localized near the void. Orientation C [1 1 0] indicates that the dislocations were organized in vein-like structures in some parallel bands along the $[\bar{1}\,1\,0]$ direction, very similar to the dislocation structures observed experimentally by Zhang [28]. In the case of Orientation D, with loading applied in the [1 0 1] direction, the crystal

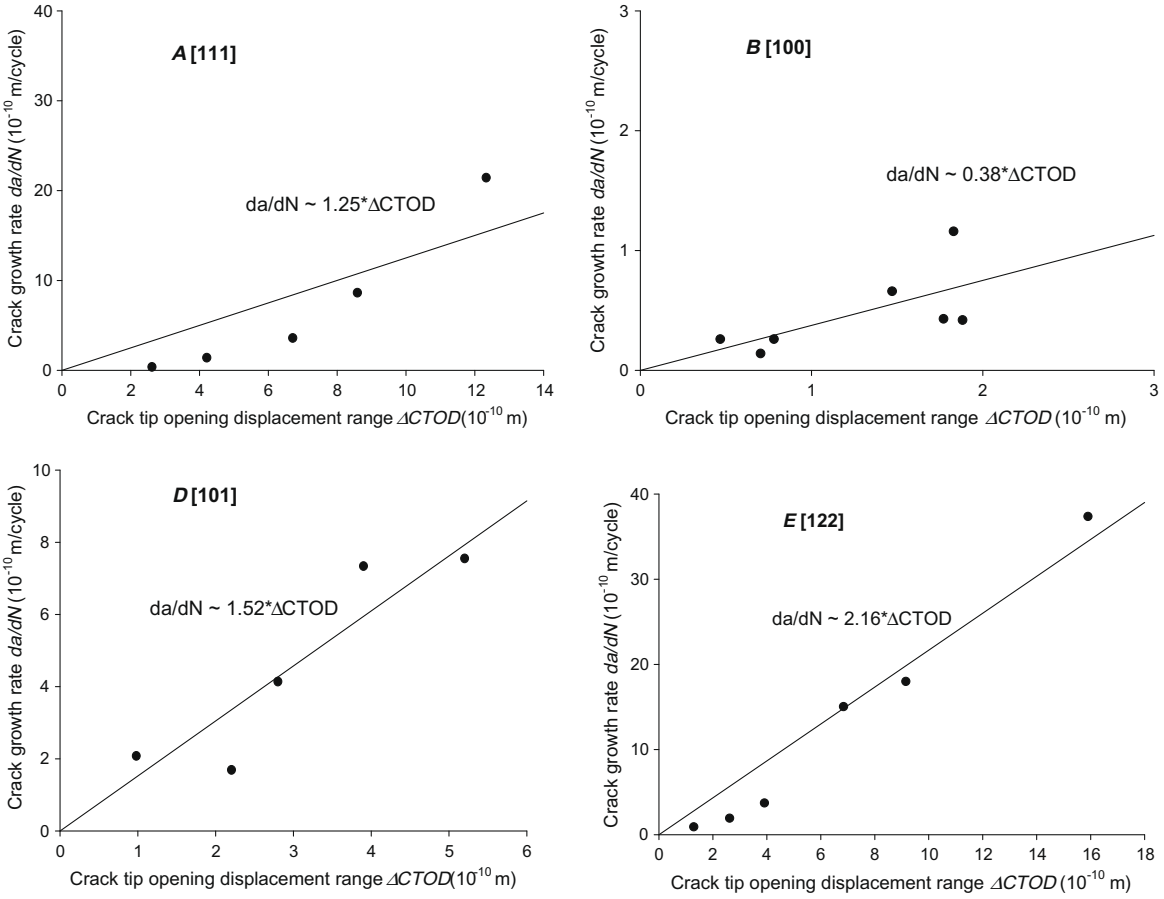

Fig. 14. Representation of crack growth rate (da/dN) versus cyclic crack tip opening displacement (ΔCTOD) for orientations A [1 1 1], B [1 0 0], D [1 0 1] and *E* [1 2 2].

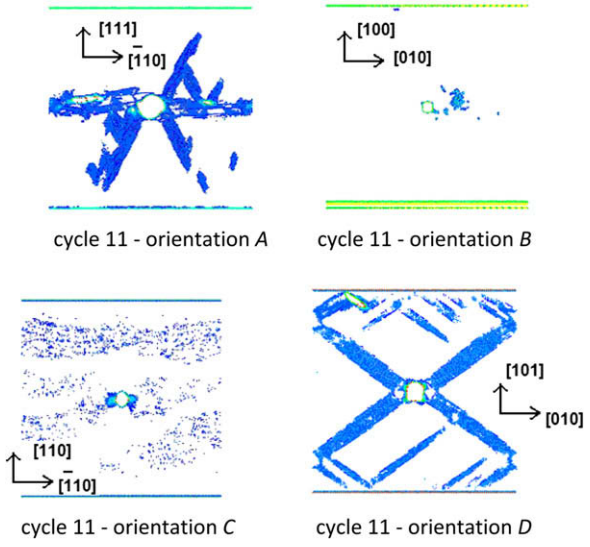

Fig. 15. Plastic slip patterns in nickel single crystal near a small circular void during fatigue loading at constant strain amplitude with $\varepsilon_{max} = 0.005$ and $\varepsilon_{min}/\varepsilon_{max} = 0.5$. All plots were taken at a 0.0045 applied strain during unloading, except the plot for Orientation B that was taken during loading.

experienced a double slip pattern. Most plastic deformation in this orientation is localized in the shear bands emanating from the void. Smaller voids and crack-like voids are nucleated in the vicinity of the main void as a result of the intense plastic deformation in the shear bands, phenomenon also observed experimentally by Zhang [28]. The cyclic stress–strain curves for the first eleven cycles are shown in Fig. 16. A dominant feature of all orientations is that for the first nine cycles, the plastic deformation was very small, but still noticeable in the change of the overall slope of the stress–strain behavior and some plastic energy dissipated during the hysteresis loops of the loading and unloading during each cycle. For all orientations, beginning with Cycle 10, a sudden increase in the slope of the stress–strain behavior was observed, as a result of the plastic strain localization in dislocations bands. Nickel single crystals in Orientation A exhibited triple slip substructures resulting in the largest stress 14 GPa in Cycle 10 at the peak strain. The smallest stress arose from Orientation B to about 9.9 GPa in Cycle 10. From Fig. 16 it can be concluded that after the first fatigue cycles, the onset of significant plastic deformation occurred very suddenly with a stress burst during the tenth loading cycle. The crystal orientation determined the configuration of dislocation structures in the shear bands, but it had no influence on the cycle at which the single crystal experienced the first large increase in stress hardening.

3.1.3. Comparison between fatigue-crack growth in copper and nickel single crystals

Comparison between all orientations for nickel and copper are shown in Fig. 17. The results indicated that the crack growth rate was highly dependent on the orientation of both crystals. For the first six cycles when the crack was small, and it did not enter yet the zone where the edge effect was dominant, the largest crack growth rate was experienced by Orientation C [1 1 0]. In this case,

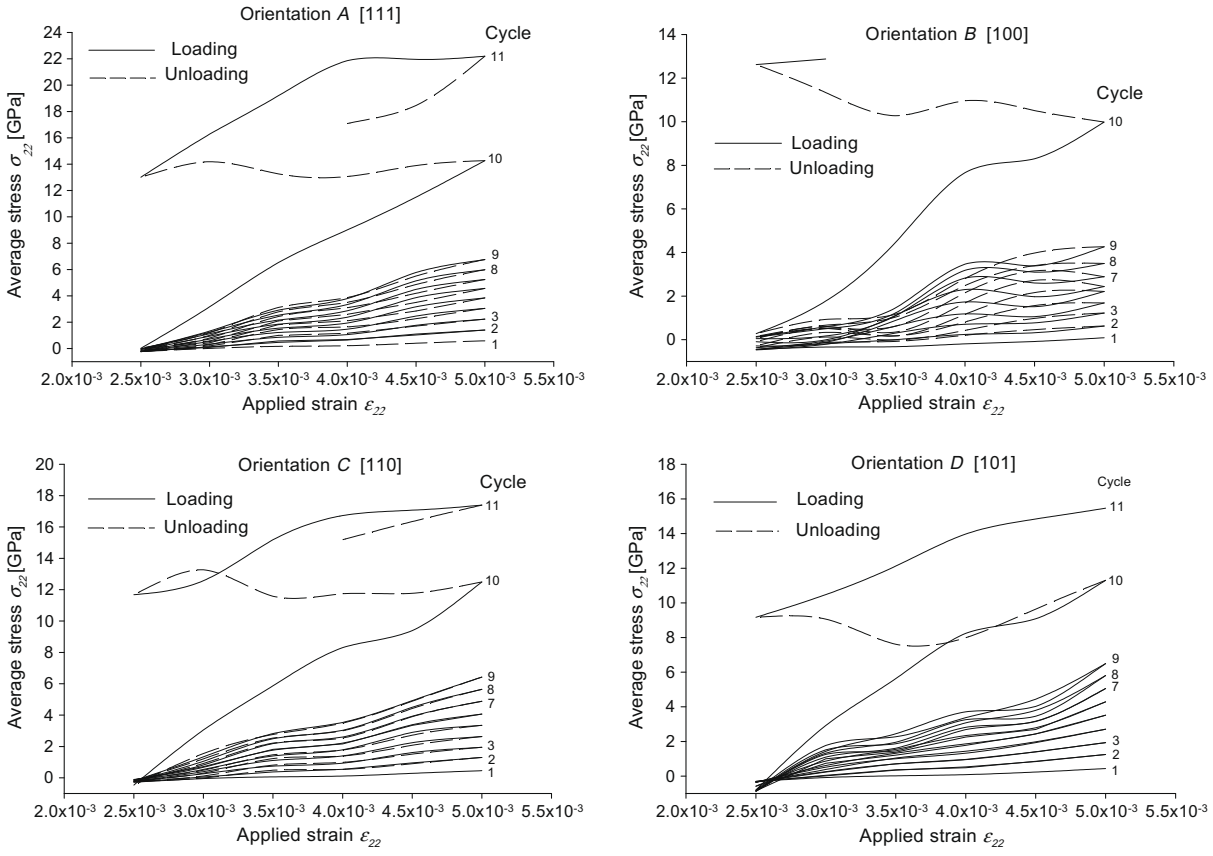

Fig. 16. Cyclic stress–strain curves for the nickel specimens indicated in Fig. 1. The loading was cyclic at constant strain amplitude with $\varepsilon_{max} = 0.005$ and $\varepsilon_{min}/\varepsilon_{max} = 0.5$.

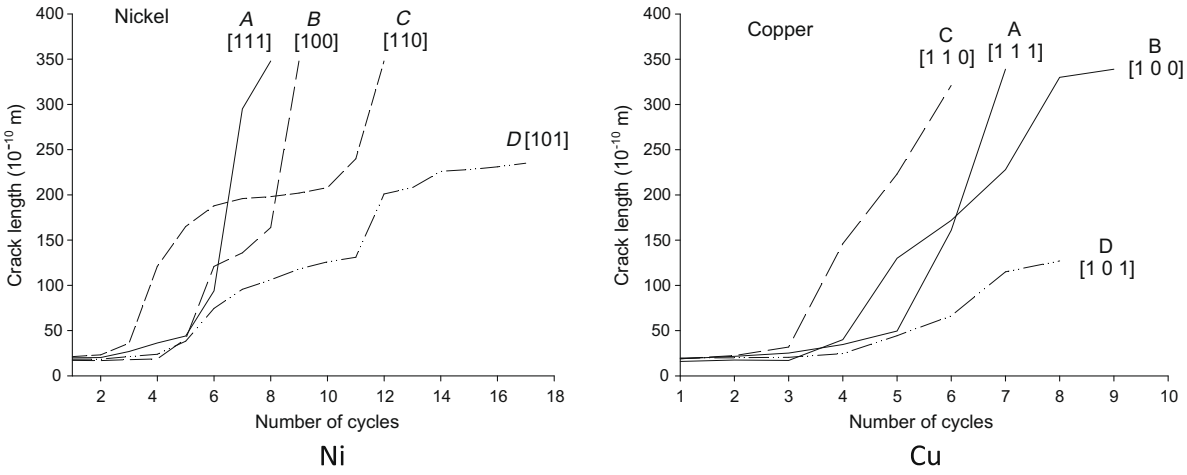

Fig. 17. Variation of total crack length with number of cycles. Comparison between different crystal orientations.

the rapid crack growth can be associated with the very little crack tip blunting observed. The smallest crack growth rate for both nickel and copper is shown by Orientation D [1 0 1]. By comparing the crack growth rates of individual orientations in Fig. 18, it can be observed that copper exhibited crack growth rates larger than nickel. When the loading was oriented in the [1 1 1] direction, both nickel and copper experienced double slip structures with the shear bands symmetrically oriented with respect to the loading direction. The third shear band along $[\bar{1}\ 1\ 0]$ observed in the case of fatigued nickel near a small circular void, was not observed very significant in the crack growth simulations; however, the crack maintained a planar configuration, propagating along this third shear direction. The [1 0 0] orientation revealed a planar crack propagation in the case of nickel with small voids nucleating in front of the crack that were coplanar with the crack, while copper single crystals experienced void nucleation at 45° from the horizontal direction around the crack tip. In the [1 1 0] orientation the void formation was not significant for the fatigue crack propagation mechanisms. The crack tip did not experience significant blunting, and the propagation mechanism involves mainly tearing

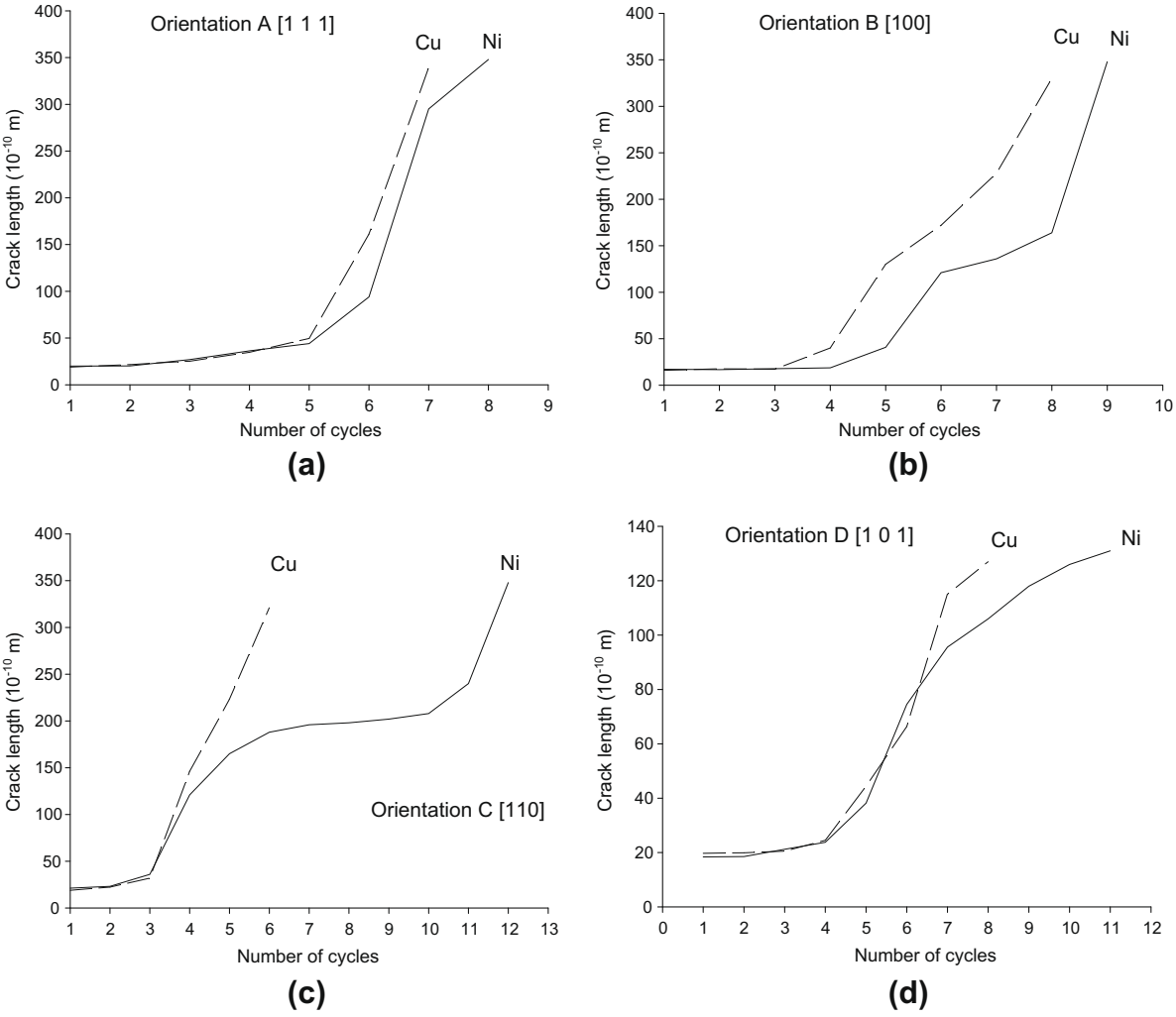

Fig. 18. Comparison of crack growth with number of cycles between nickel and copper single crystals for each Orientation A–D.

of atomic bonds in the crack plane at the crack tip. For this orientation, the crack advance was very rapid compared with other orientations, especially in the first six cycles when the influence of the specimen edges were not significant. Orientation [1 0 1] indicated for both nickel and copper the smallest amount of crack growth. The crack tip experienced an evident double slip pattern with consequential shear bands in the vicinity of the crack.

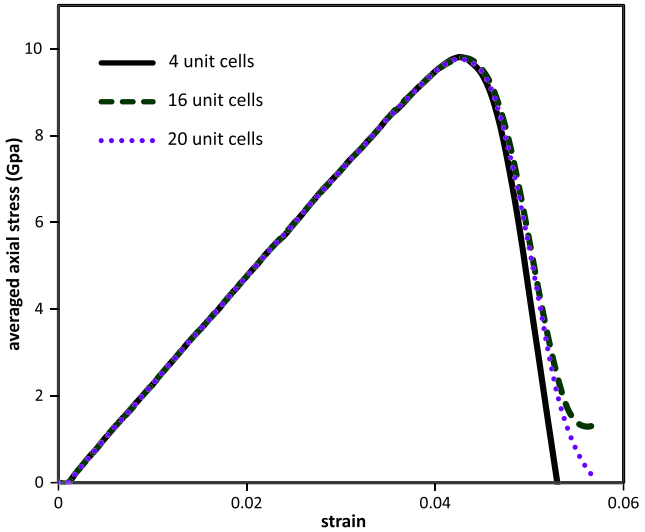

Fig. 19. Averaged stress strain curves from Orientation C [1 1 0] loading direction of various thicknesses in *z*-direction.

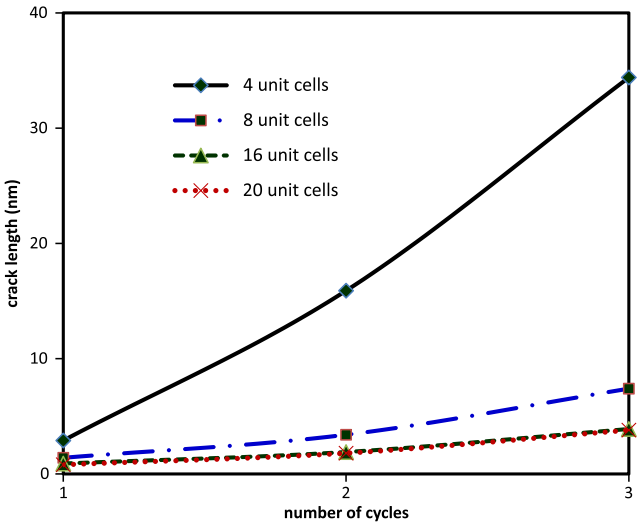

Fig. 20. Variation of fatigue-crack growth with number of cycles from Orientation C of various thickness in *z*-direction.

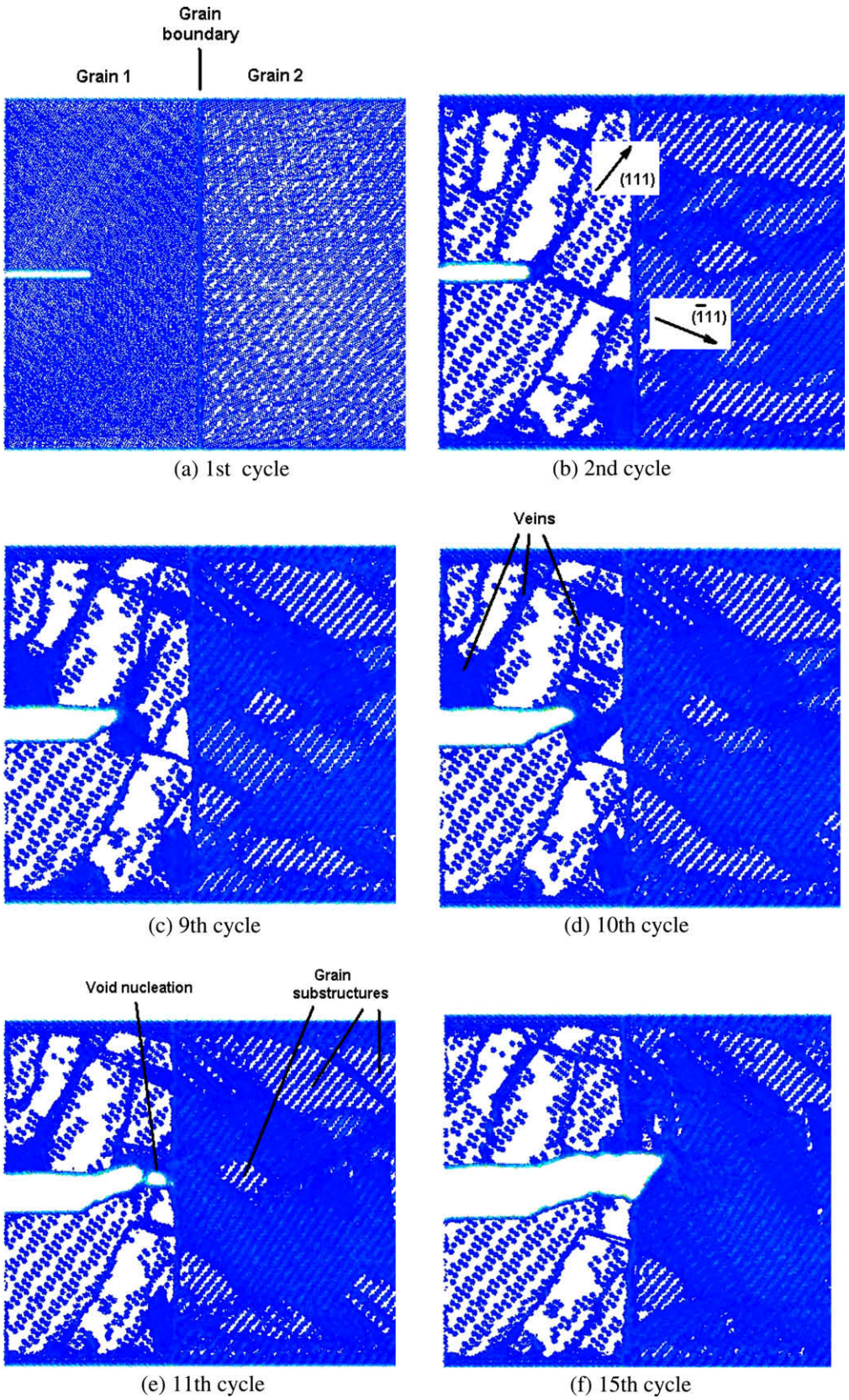

Fig. 21. Simulation of fatigue crack growing toward the grain boundary for the bicrystal AA. The formation of veins or regions with large concentration of dislocations is illustrated.

3.2. Fatigue-crack growth in bicrystals

Grain boundaries play an essential role in determining the resistance of fatigue crack propagation in materials [33,26,20,36]. In this section, the influences of grain boundary on the fatigue-crack growth in copper and nickel bicrystals were investigated. The MEAM potential was used for copper, and the EAM potential was used for nickel.

3.2.1. Fatigue-crack growth in copper bicrystals

Fig. 21 illustrates the fatigue-crack growth process for the first tilt grain boundary AA. Fig. 21a shows the initial configuration of the specimen. Starting at Cycle 2, the crack tip blunted and developed two distinct slip bands at the crack tip. The upper slip band was formed by plastic shear on the primary slip system $[1\,0\,\bar{1}](1\,1\,1)$. The angle between the trace of this slip system on the view plane $(1\,\bar{2}\,1)$ and the vertical tensile axis $[0\,1\,2]$ is 50.76°. The lower slip band is due to plastic slip on the conjugate slip system $[1\,0\,\bar{1}](1\,1\,1)$. The trace of this slip system on the plane of view $(1\,\bar{2}\,1)$ is the $[3\,2\,1]$ direction and forming a 61.41° angle with the vertical axis. At Cycle 9, the crack deviated along the primary slip band into a mixed Mode I + II crack growth. At Cycle 10, due to the stress concentration effect of the grain boundary, the two slip bands active at the crack tip became more diffuse, with the crack tip plasticity being spread out more evenly around the crack tip. At Cycle 11, near the grain boundary void nucleation was observed in front of the crack tip in the region with a fairly high density of dislocations. The nucleated void joined back with the main crack and induced the crack propagation into the adjacent grain. Large crack tip blunting was observed at the passage of the crack into the second grain. During loading from Cycle 2 to Cycle 15, the development of grain substructures occurred in the specimen. SBs formation along the primary slip system was observed in the first grain. The SBs were parallel to the primary slip directions. Also, regions with high and low dislocation densities were observed in the specimen after Cycle 10. The second grain also experienced substructuring in dislocation cells, mainly in the beginning of the fatigue process while the crack was still in the first grain.

In Fig. 22 the simulation results of the second grain boundary misorientation BA are shown. From the loading conditions and the orientation of the crystalline lattice in the two grains, crack propagation was more difficult as the crack moved toward the grain boundary. At the left edge of the specimen, the crack experienced partial closure. Some important dislocation substructures developed in the two grains. In the first grain, a slip band at the same orientation as in the case of grain boundary tilt AA was observed. This slip band was caused by plastic slip along the primary slip system $[1\,0\,\bar{1}](1\,1\,1)$. Around the crack tip, different stress states can be identified in Fig. 22a. Behind the crack tip, regions with vacancies and veins can be identified. At the grain boundary, voids nucleated at the interface between the two grains. In the second grain, slip bands nucleated from the grain boundary along the slip system $[1\,0\,\bar{1}](1\,1\,1)$. In this case, a large concentration of dislocations at the grain boundary was observed due mainly to the difficulty of dislocations to cross from one grain to another.

The grain boundary tilt CA crack growth is shown in Fig. 23. After the first cycle, the crack developed a slip band along the primary slip system $[1\,0\,\bar{1}](1\,1\,1)$. SBs also formed in the specimen parallel to each other and in the general direction of the primary slip system. Outside the SBs, the density of dislocations was very small. Due to the easy transfer of dislocations across the grain boundary, the density of dislocations at the interface between the two grains was very small. The formation of veins and the increase in their volume fraction with applied loading was another noticeable feature for boundary tilt CA. No deviation of crack path out-of-plane was recorded. For the cases of grain boundary tilt AA and CA, the orientation of the first grain from which the crack originated was the same. The difference between the two cases was the orientation of the second grain. By comparing these two cases AA and CA (Figs. 21 and 23), we draw the conclusion that long before reaching the grain boundary, the crack tip plasticity and implicitly the kinetics of crack growth was influenced by the orientation of the adjacent grain. In the CA boundary tilt, as opposed to AA, the dislocations easily crossed the grain boundary. As no slip band formation occurred at the crack tip, and thus, no crack deviation out-of-plane was experienced by the crack. In addition, because the grain boundary did not create any difficulty for dislocations to pass through (relatively low intergranular constraint), no grain substructuring was observed in the case CA as opposed to case AA. During the crack propagation, the crack plane showed distinctive fatigue striations as recorded by the crack position at different cycles.

In the case of grain boundary tilt DD shown in Fig. 24, two slip bands formed at the crack tip. The upper slip band was created by plastic slip along the primary slip direction $[1\,0\,\bar{1}](1\,1\,1)$, while the lower slip band was caused by plastic shear along the secondary slip direction $[1\,0\,1](1\,1\,\bar{1})$. Comparing grain boundary tilt AA with DA (Figs. 10 and 13), one can compare the difference between them. Even though the orientation for the first grain was the same, different conjugate slip systems were activated to create the lower slip band at the crack tip. Given the same orientation of the initial cracked grain, due to the different intergranular constraint induced by the adjacent grain, different slip systems can be activated at the crack tip to create the conjugate slip band. After approximately eleven cycles for Orientation DA, the crack deviated from a Mode

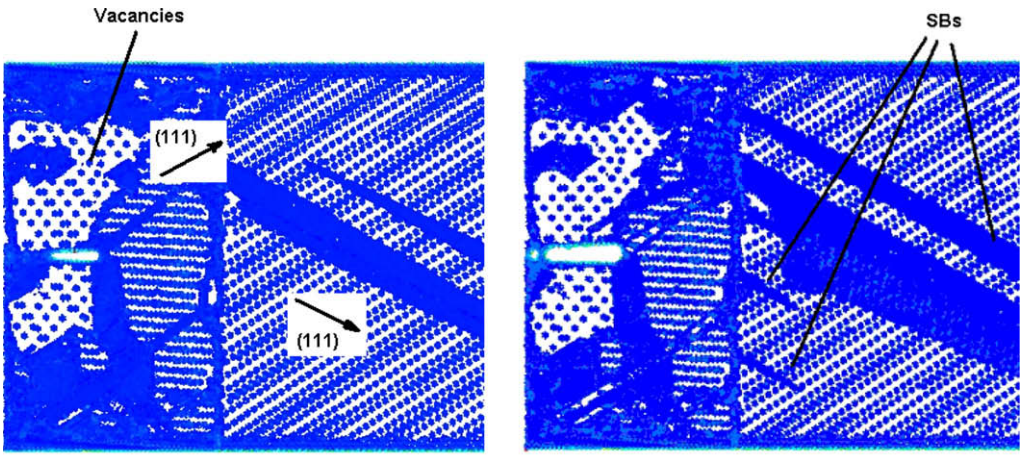

Fig. 22. Simulation of fatigue crack growing toward the grain boundary for the bicrystal BA. Formation of vacancies (atoms displaced from their equilibrium position), and narrow regions as slip bands (SBs) undergoing intense plastic deformation is illustrated.

I crack growth into a mixed Mode I + II along the primary slip direction due to a larger Schmid Factor on the primary slip band as compared with the corresponding value for the conjugate slip band. As the crack grew near the grain boundary, at Cycle 12, a void nucleated at the bicrystal interface, causing the crack to change directions. For the grain boundary tilt DA, the SBs were generally oriented along the primary slip direction $[1\,0\,\bar{1}](1\,1\,1)$, with the familiar ladder-like structuring of dislocations within two SBs. Outside the SBs, the dislocation density was very low, leading to an increased hardness of the matrix material compared with the softer material within the SBs. As in the case of other grain boundary tilt cases, the DA interface subjected to fatigue loading developed veins, which induced greater volume fractions as fatigue damage accumulated. A summary of the main findings from the fatigue-crack growth simulations in bicrystals is presented in Table 2.

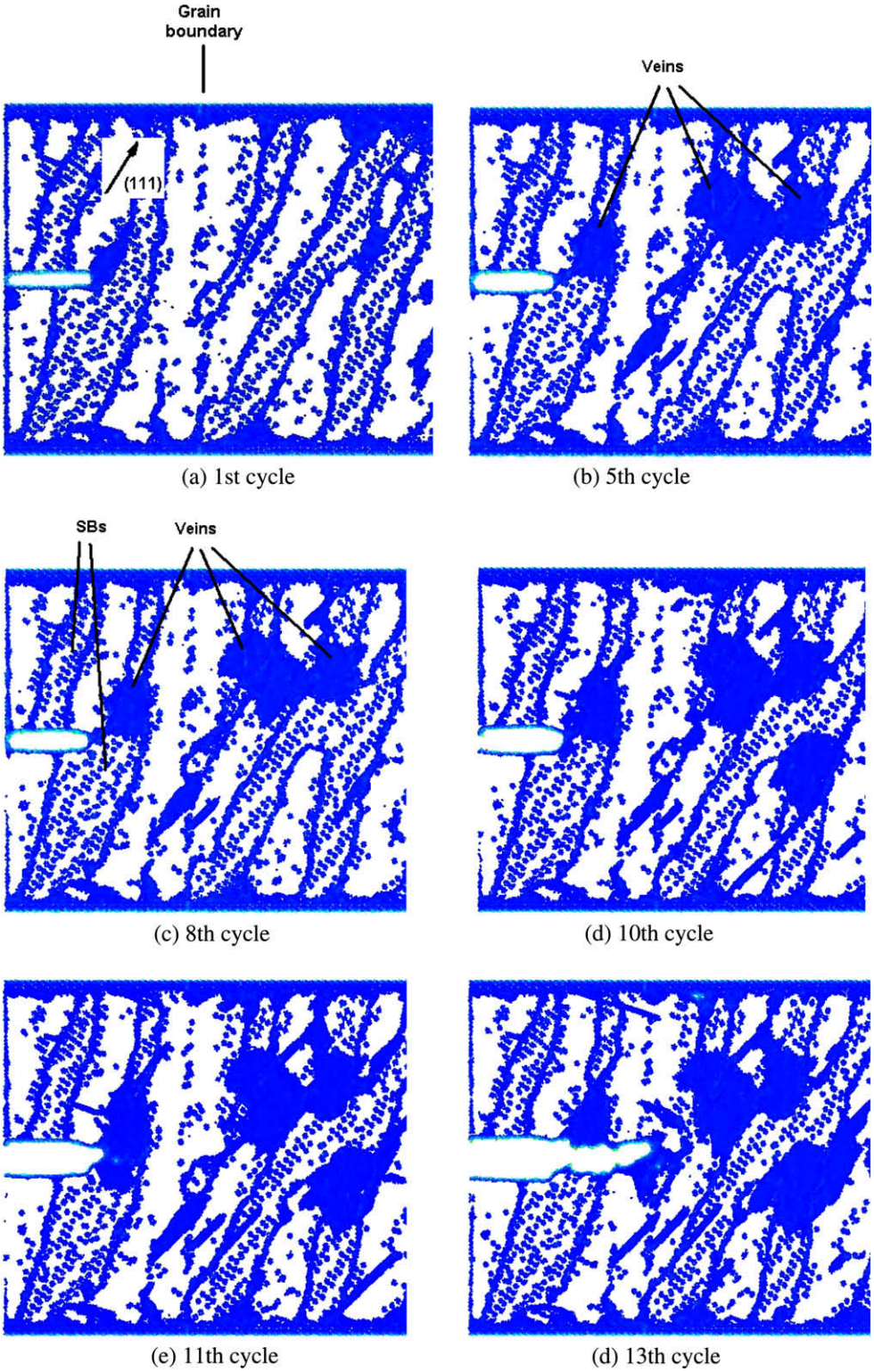

Fig. 23. Simulation of fatigue crack growing toward the grain boundary for the bicrystal CA.

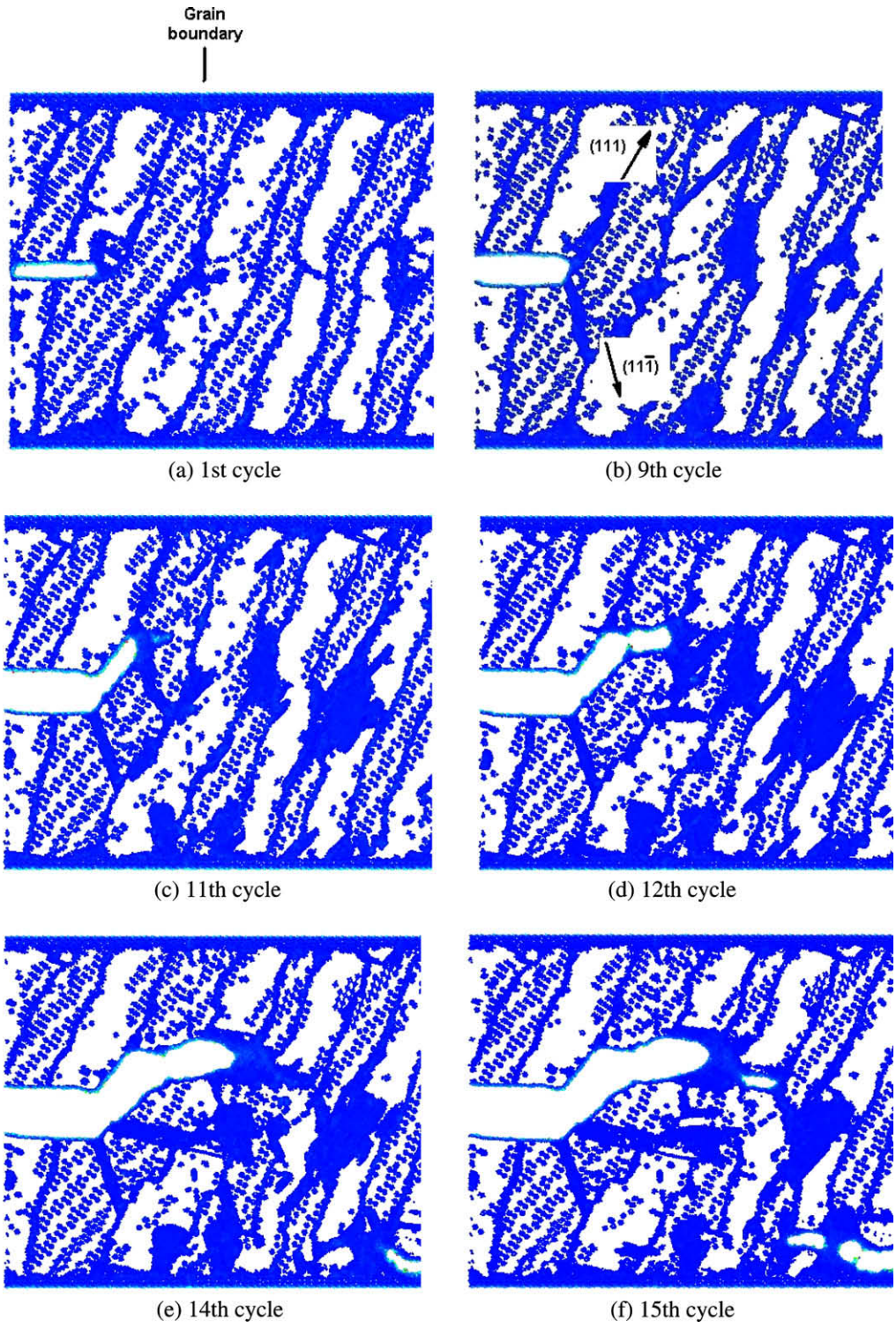

Fig. 24. Simulation of fatigue crack growing toward the grain boundary for the bicrystal DA.

Table 2
Summary of fatigue-crack growth data in bicrystals.

Grain boundary tilt	Misorientation (degree)	Dislocation structures	Propagation mode	Crack extension mechanism
AA [0 1 2]/[1 1 1]	39.23	Grain substructuring, veins, slip bands	Mode I + II	Ductile
BA [0 1 2]/[$\bar{3}$45]	55.77	Slip bands, vacancies	–	–
CA [0 1 2]/[0 1 2]	37.39	Veins, slip bands	Mode I	Ductile
DA [0 1 2]/[0$\bar{1}\bar{2}$]	60	Veins slip bands	Mode I + II	Ductile

3.2.2. Fatigue-crack growth in nickel bicrystals

The simulation of fatigue-crack growth in bicrystal with a large misorientation and the corresponding single crystal are shown in Figs. 25 and 26, respectively. These figures show that the crack was impeded by the grain boundary in the bicrystal. Figs. 27 and 28 show the fatigue crack propagation in the bicrystal with a small misorientation and the corresponding single crystal, respectively. In the bicrystal, the crack can go through the grain boundary, but its growth rate was obviously lowered by the grain boundary.

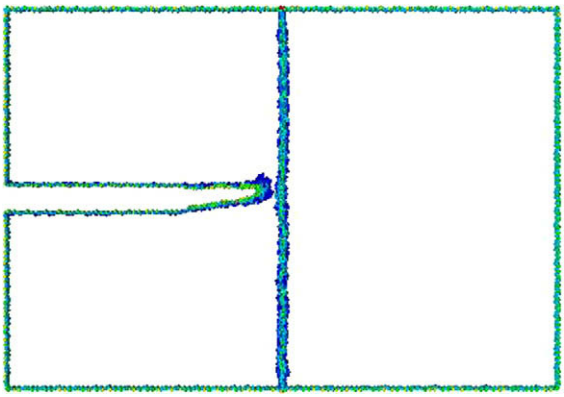

Fig. 25. Simulation of fatigue-crack growth toward grain boundary for $\theta = 30^\circ$ at 13th cycle. The crack stops growing in front of the grain boundary at 5th cycle.

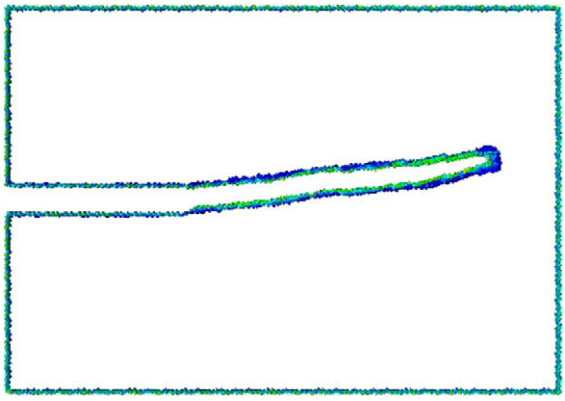

Fig. 26. Simulation of fatigue-crack growth in corresponding single crystal for $\theta/2 = 15^\circ$ at 13th cycle.

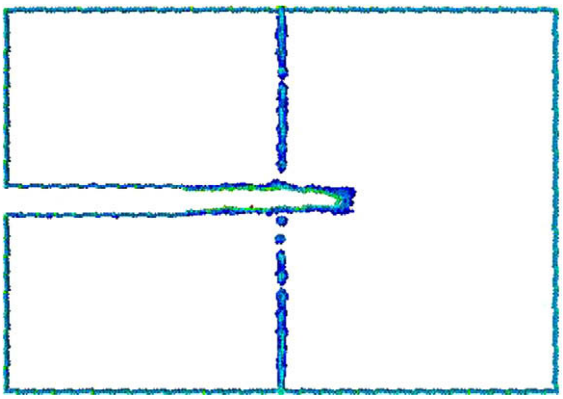

Fig. 27. Simulation of fatigue-crack growth toward grain boundary for $\theta = 10^\circ$ at 13th cycle.

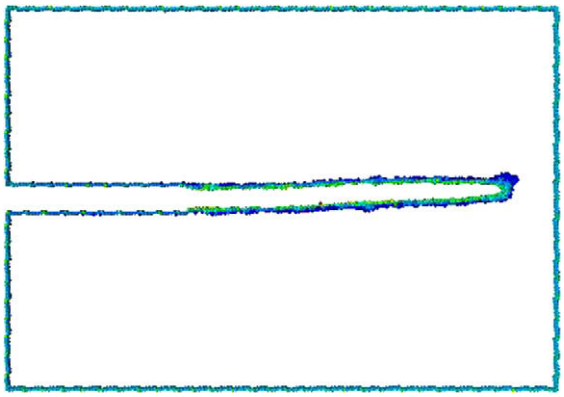

Fig. 28. Simulation of fatigue-crack growth in corresponding single crystal for $\theta/2 = 5^\circ$ at 13th cycle.

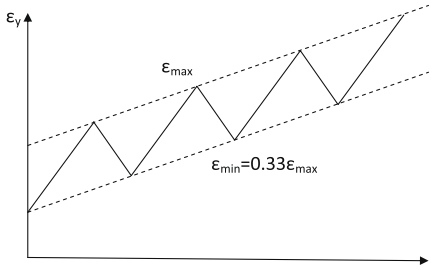

Fig. 29. Increasing maximum strain loading.

3.3. Fatigue-crack growth in nanocrystalline

3.3.1. Fatigue-crack growth in nanocrystalline copper

Figs. 30–32 illustrate the evolution of fatigue-crack growth for the nanocrystalline cu specimen containing five grains. Fig. 30 shows the centrosymmetry parameter, and Fig. 31 shows the associated uniaxial Green strain illustrating the fairly large local strains (50%) at the grain boundaries near the crack tip; Fig. 30a also shows the initial configuration of the specimen. The crack propagated along persistent slip bands within the grain. At the sixth cycle, it encountered the grain boundary. Then the crack propagated along the grain boundary and traversed into another grain. The crack growth in the specimen with 20 grains is illustrated in Fig. 33. The crack grew within the grain by the mechanism of atomic cleavage. It encountered the triple point of grain boundaries at the fourth cycle. After that, the crack propagated along grain boundary.

Fig. 34 shows the simulation results in the specimen containing 40 grains. The crack also propagated along a persistent slip band within the grain. When the crack reached grain boundary, it stopped growing due to the resistance of grain boundary. In all of the cases, the formation of the dislocation structure due to cyclic loading was observed in different grains. The crack propagated along grain boundaries when the angle between the direction of crack propagation and the grain boundary was small, while it was impeded by the grain boundary when the angle was large. Hence, the tortuosity of the fracture path is a function of the crystal orientations, local misorientations between grains, and grain size.

3.3.2. Fatigue-crack growth in nanocrystalline nickel

The crack propagation of nanocrystalline nickel is shown in Fig. 35, where the position of the crack tip is plotted as a function of the number of cycles. The slopes in this type of plot were

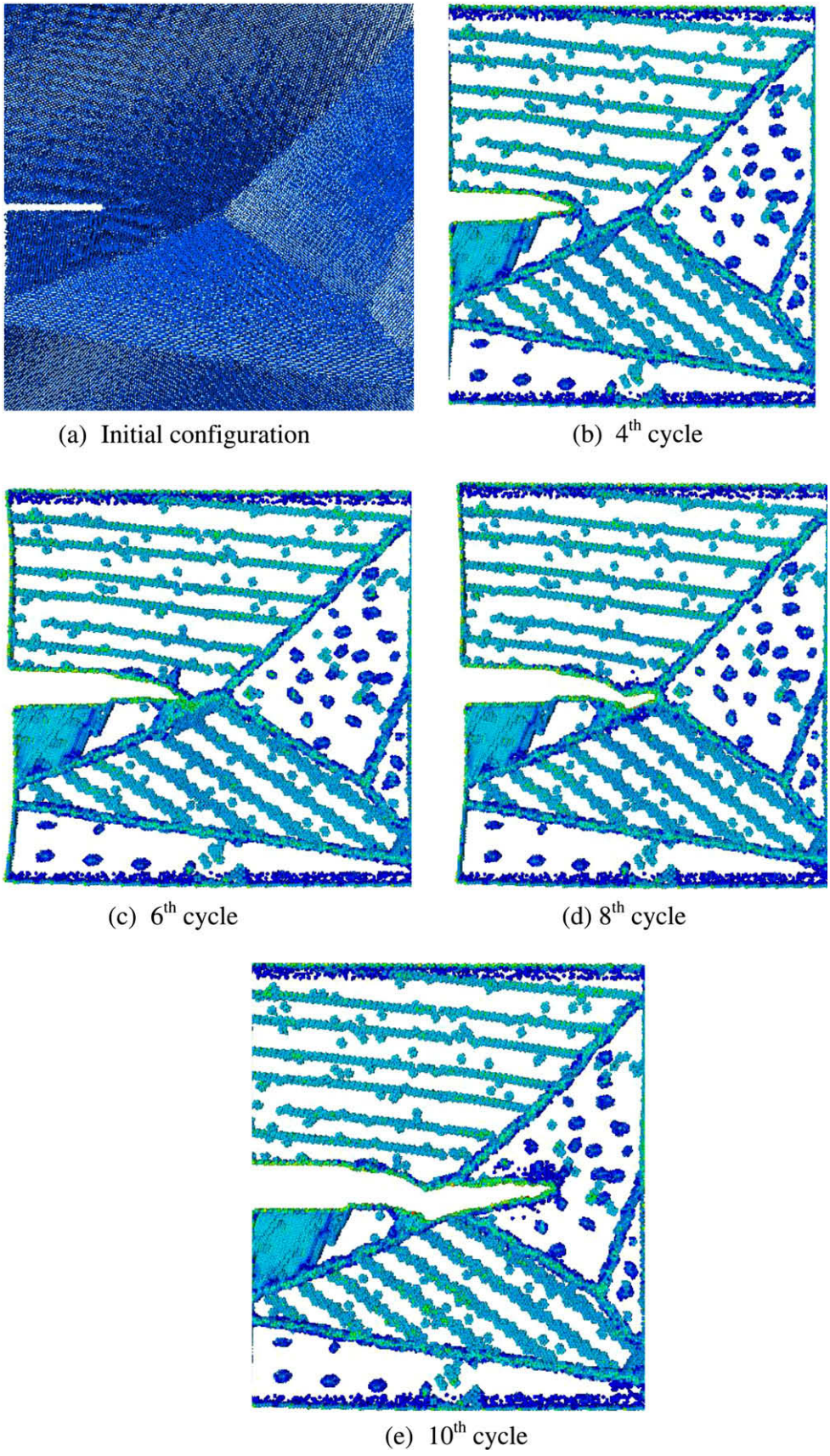

Fig. 30. Centrosymmetry parameter is shown for the simulation of fatigue-crack growth in polycrystal containing five grains for nanocrystalline copper.

computed for each of the stress intensity amplitudes considered. Fig. 36 shows the resulting rates of crack advance calculated using molecular dynamics for the three values of the stress intensity amplitude. The figure also shows the results of molecular statics

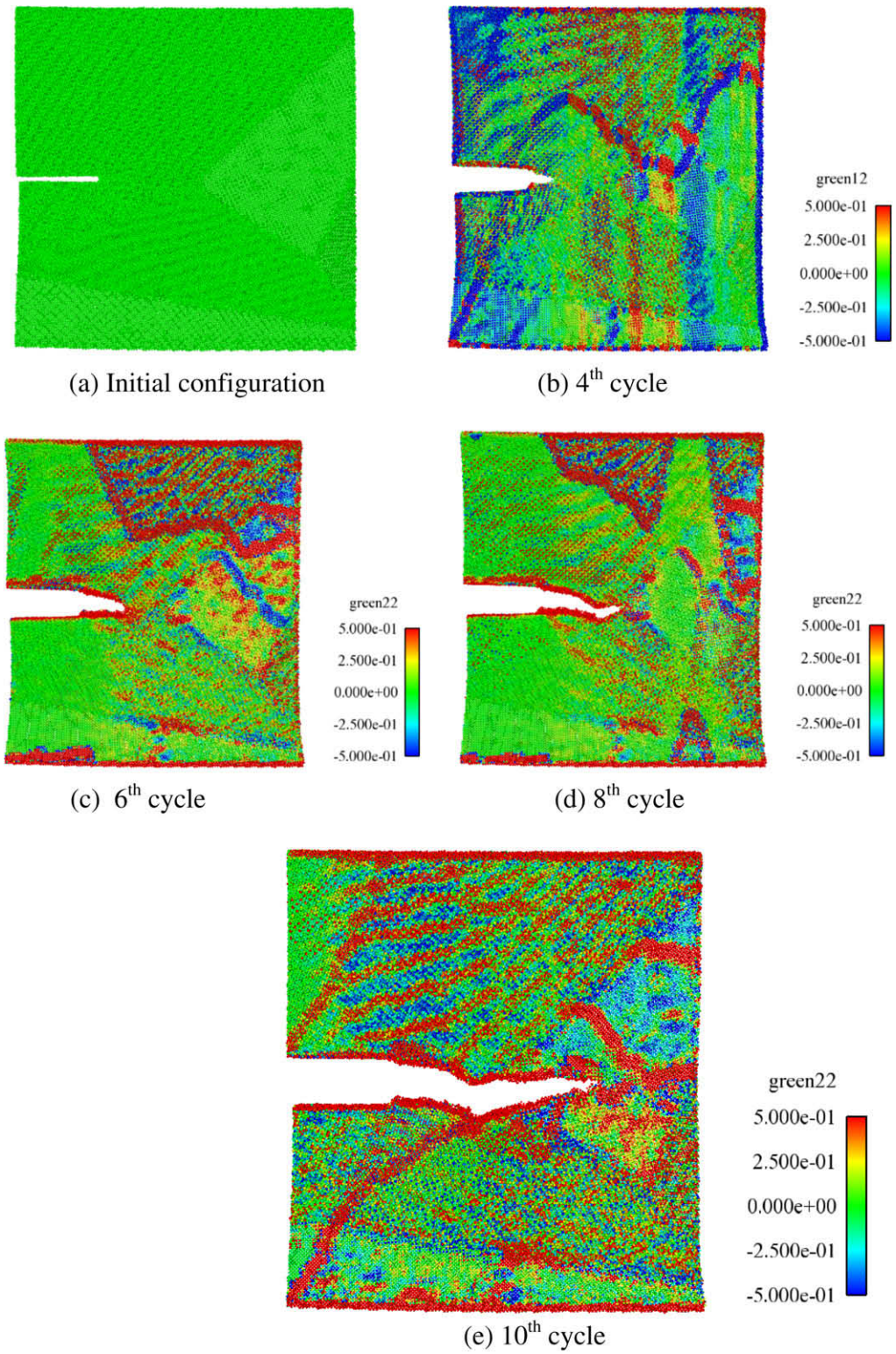

Fig. 31. The uniaxial strain component (Green strain 22) is shown for the fatigue-crack growth in polycrystal containing five grains for nanocrystalline copper. Note the strains near the grain boundaries.

and the available experimental data for nanocrystalline Ni by Hanlon et al. [37].

The results show that crack advance rates are not very sensitive to the technique as the molecular dynamics and molecular statics giving similar results. This suggests that the molecular dynamics results do not have major spurious effects due to the unrealistically high loading rates. To further establish confidence in these results, we studied the basic mechanisms of crack advance using both techniques. For both cases, we observed a continuous increase in the number of dislocations present in the crack tip region as the crack advanced, and the formation of nanovoids or vacancy clusters ahead of the main crack. Fig. 37 shows the number of disloca-

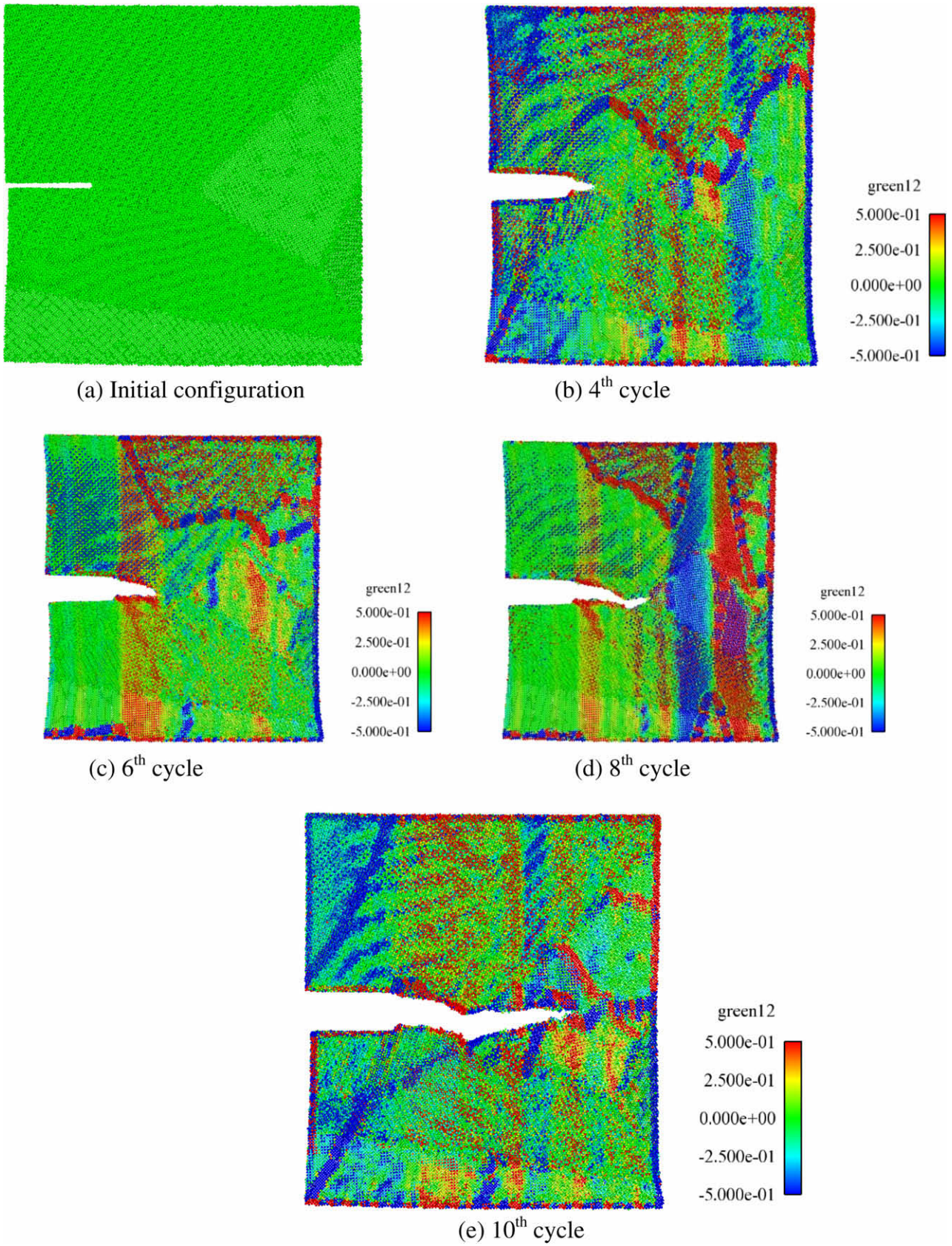

Fig. 32. The shear strain component (Green strain 12) is shown for the fatigue-crack growth in polycrystal containing five grains for nanocrystalline copper. Note in Cycle 8 the crack path oriented toward the local shear strain.

tions and nanovoids observed as the cyclic deformation progressed. Fig. 38 shows crack tip configurations corresponding to Cycles 1, 12, and 20. The simulations shown in Figs. 37 and 38 were conducted using molecular statics at a stress intensity amplitude of

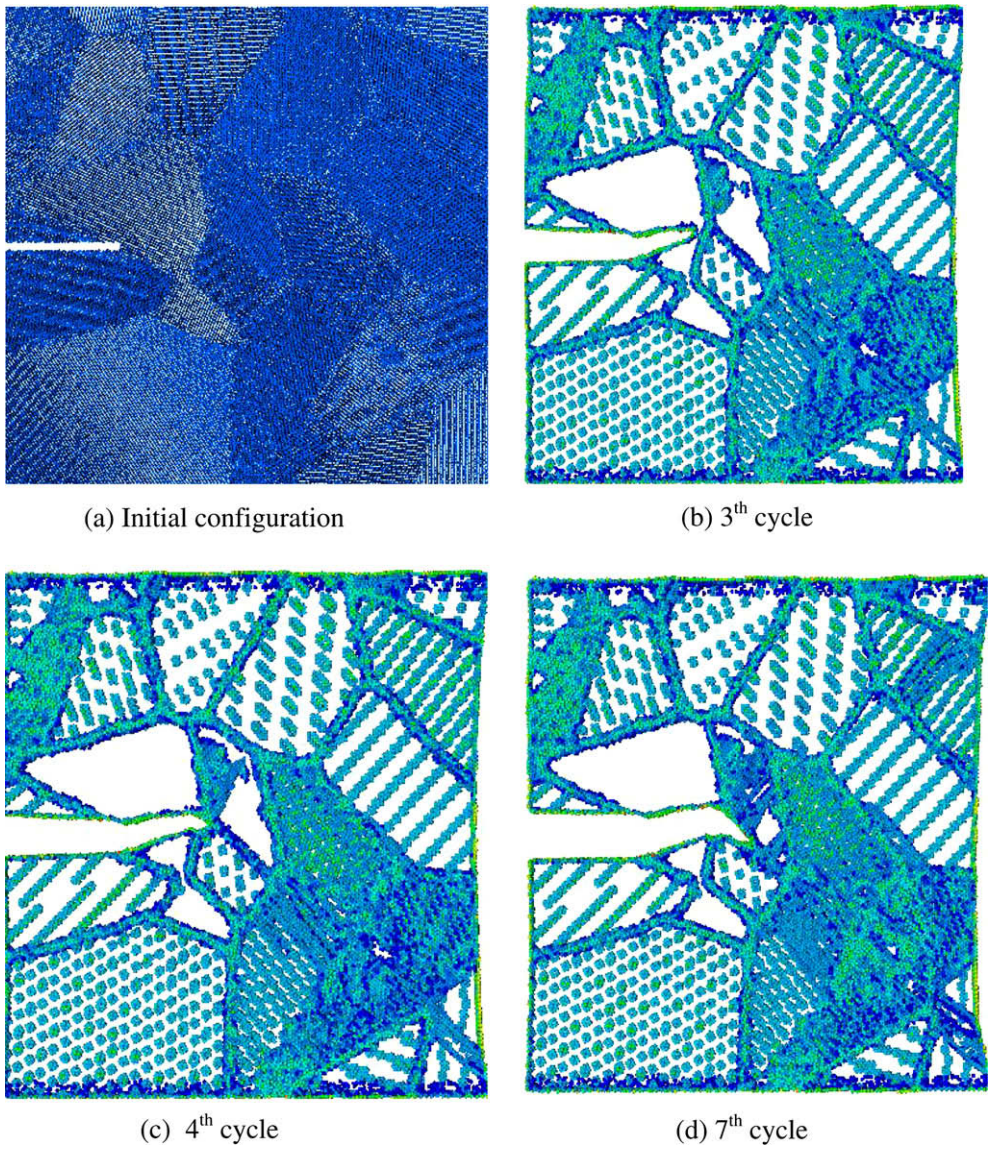

Fig. 33. Centrosymmetry parameter for the simulation of fatigue-crack growth in polycrystal containing 20 grains for nanocrystalline copper.

1.28 MPa $\sqrt{\text{m}}$. Frames on the left side of Fig. 38 are for maximum loading conditions, whereas frames on the right show the minimum loading configurations. The visualization in Fig. 38 is carried out using the local hydrostatic stress calculated for each atom. The gray scale shows areas under tension as light gray and areas under compression in darker shades. The visualization technique requires an assumption regarding the local atomic volume for each atom, which we considered constant. The technique allows the visualization of the damage, including stacking faults that are the result of the emission of partial dislocations from the grain boundaries.

In Fig. 39 we show greater detail of the configuration of the tip as the crack is loaded to the maximum stress intensity after 26 and 31 cycles. The main mechanism of crack advance is the formation of vacancy clusters ahead of the crack tip that result from the plastic deformation in the tip region. The results in this figure were obtained using a static technique where the crack reached local equilibrium at both the high and the low loading points of each cycle. The results obtained using molecular dynamics were similar in nature, also showing the formation of nanovoids ahead of the main crack. This mechanism of the crack advance was also observed in the monotonic fracture simulation studies of Ni that we carried out previously [18]. We note that crack advance and the formation of the nanovoids under monotonic loading occurred at stress intensity amplitudes that were two to three times higher than those used here as the maximum loading. The formation of nanovoids in a grain boundary ahead of the main crack seems to be a general failure mechanism in nanocrystalline materials depending on the orientation as evidenced in the copper as well. In the present simulations we find that these nanovoids were created by the presence of dislocations emitted from the crack tip. In Fig. 39 we can see nanovoids both within the grain where the crack tip was located and at the grain boundary. The nanovoids within the grain were related to the presence of two or more dislocations in adjacent planes. The arrival of the dislocations to the grain boundary region also caused the formation of nanovoids, as the dislocations could not cross into the adjacent grain. We observed a distribution of these nanovoids that was essentially confined to the grain where the crack tip was located, with most of the dislocations being unable to continue to glide across the grain boundaries.

It is encouraging to note that our results yield four points in the curve of crack advance versus stress intensity amplitude that are very consistent with the experimental measurements in nanocrys-

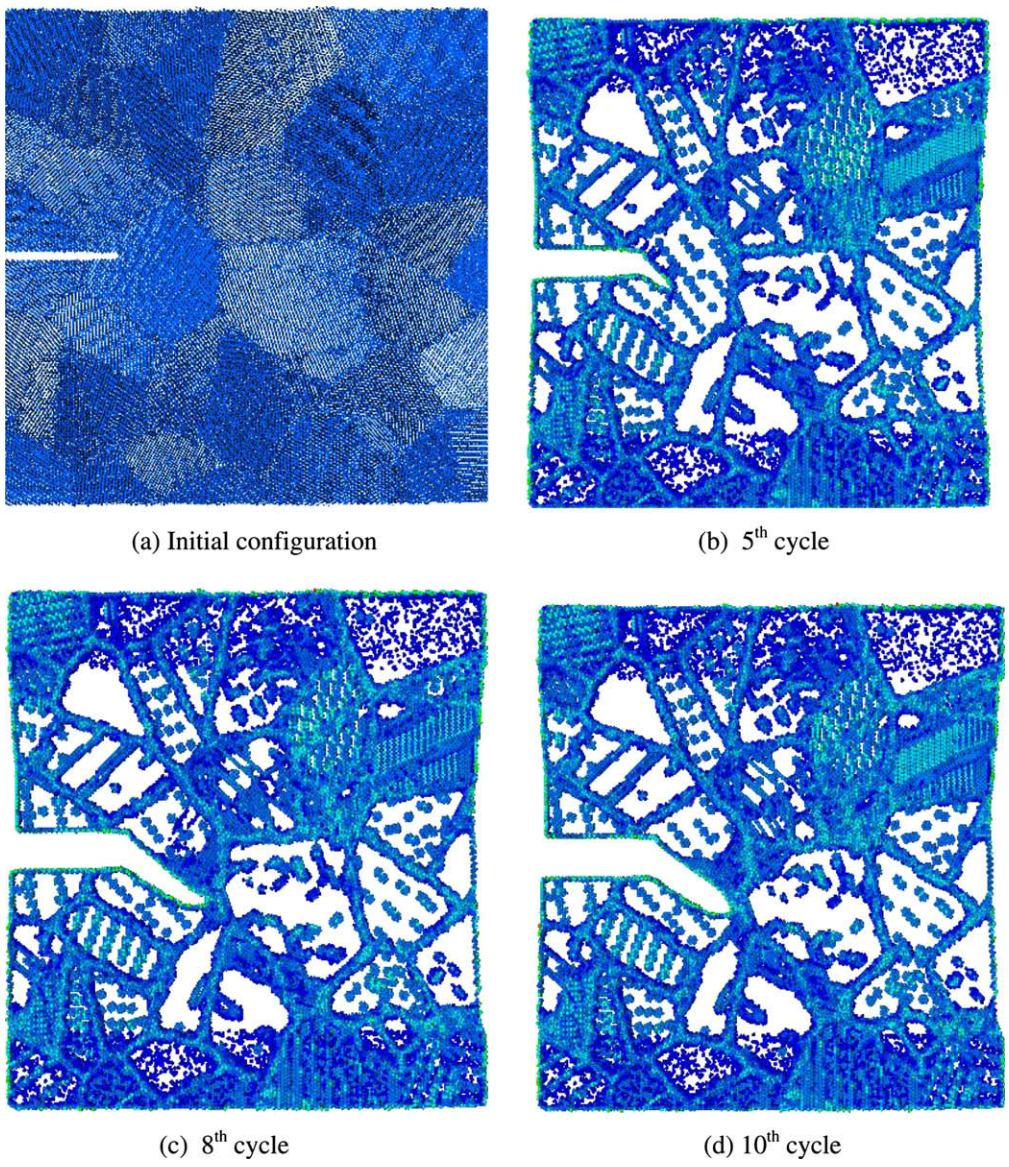

Fig. 34. Centrosymmetry parameter for the simulation of fatigue-crack growth in polycrystal containing 40 grains for nanocrystalline copper.

talline Ni. The results as illustrated in Fig. 36 show that our simulations are in the Paris Law regime. This can be related to the small size scale of the microstructural features in our sample. The size of our cyclic plastic zone is comparable to the grain size, as shown in Fig. 38, the point where a transition to a Paris regime typically occurs [38]. Our results imply a Paris Law exponent of about two, indicated by the line in Fig. 36. This exponent is expected from

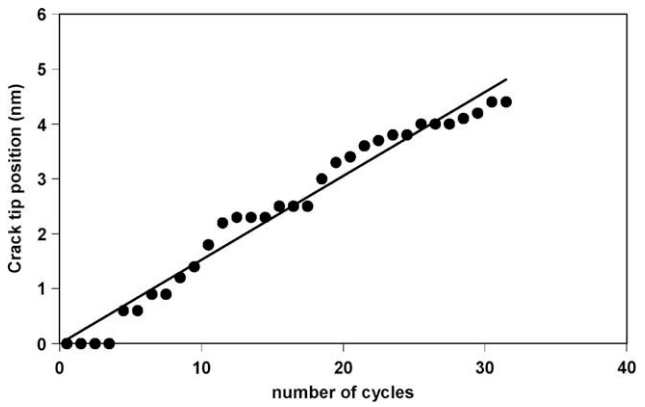

Fig. 35. Crack advance as a function of the number of cycles observed in a static simulation with $\Delta K = 1.28$ MPa $\sqrt{m}$.

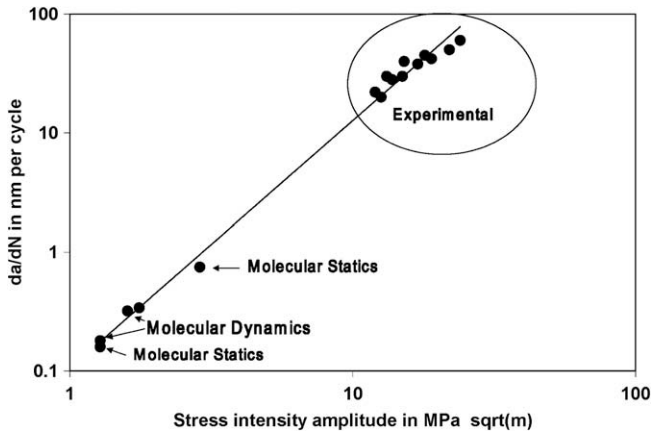

Fig. 36. Rate of crack advance for both molecular statics and dynamics simulations together with experimental results by Hanlon et al. [37].

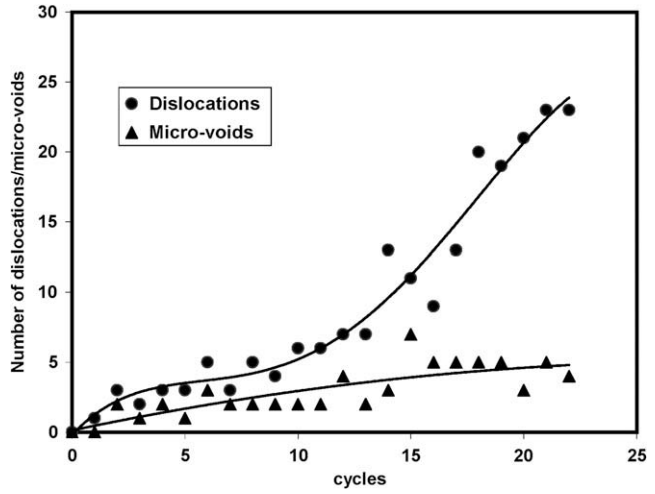

Fig. 37. The number of dislocations and nanovoids present in the crack tip region as the cyclic loading proceeds for nanocrystalline nickel.

deformation controlled geometrical models that are based on crack tip opening displacement which are related to the square of the stress intensity amplitude [38].

One Paris Law model with an exponent of two is described by Weertman [39] for fatigue-crack growth controlled by crack tip blunting. In this model, the crack growth rate is given by $da/dN = b(\Delta K/2\,g\,Kc)^2$ (Eq. (10.37) in [39]), where da/dN is the crack growth rate per cycle, b is the Burgers vector, g is the ratio between critical stress-intensity-factors for dislocation emission and cleavage, and Kc is the critical stress intensity for cleavage. Using a value of 0.9 for the ratio g, the Burgers vector of a Shockley partial dislocation of 0.144 nm and a value of 0.96 MPa $\sqrt{\text{m}}$ for Kc, we obtain $da/dN = 0.087\Delta K^2$, with da/dN in nm per cycle and the stress intensity in MPa $\sqrt{\text{m}}$. This compares well with the best fit line obtained from our four data points which is $da/dN = 0.095\Delta K^2$ in the same units. This good agreement suggests that the crack advance process observed here is controlled by crack tip blunting caused by dislocation emission. Alternatively, one can use a simpler formulation also described by Weertman [40] for a similar model which gives da/dN of the order of $(\Delta K/G)^2$. This for Ni would imply $da/dN = 0.173\Delta K^2$ in the same units, which is again of the order of our best fit values. The models that give da/dN of the order of $(\Delta K/\sigma_{\text{yield}})^2$ or $\Delta K^2/G \times \sigma_{\text{yield}}$ would significantly overestimate the current results.

To further support our conclusion that the crack advance is controlled by blunting caused by dislocation emission, Fig. 40 shows a plot of the crack tip position versus the total cumulative blunting caused by dislocation emission. The total cumulative blunting values in this figure were obtained from the total number of dislocations observed in the sample, multiplying by the projected Burgers vector. We assumed that all dislocations emitted from the crack tip caused blunting of the crack. The data in Fig. 38 indicate that the total crack advance is of the order of the total cumulative blunting that can be attributed to the dislocations observed in the sample.

Regarding the threshold stress, the values we obtained (about 1 MPa $\sqrt{\text{m}}$) also compare very well with the model estimate of $Gb_{1/2}$ [40] which gives 0.91 MPa $\sqrt{\text{m}}$. The threshold value found here also is of the order of the estimates based on dislocation dynamics models [41–44] of $3 \times 10^{-6}\,E\,\sqrt{\text{m}}$, which for a value of the Young modulus E of 200 GPa gives 0.6 MPa $\sqrt{\text{m}}$. For stress intensity amplitudes just above the threshold value, we obtain crack advance rates that are of the order of an interatomic distance, consistent with the analysis given by Weertman [40].

Although we see evidence of damage accumulation in the sample, as shown in Fig. 38, the predicted Paris Law exponent based on damage accumulation models is four [38], which does not agree with our results. This can be related to the presence of grain boundary material in the immediate vicinity of the source of dislocation emission. For the nanocrystalline materials studied here, the dislocations that are emitted from the crack tip interact with the grain boundaries present in the crack tip zone at very short distances from where they are emitted. Typically, many dislocations travel to a nearby grain boundary and are then absorbed. The grain boundaries themselves contribute to accommodating plasticity, as has been shown in many studies of deformation of nanocrystalline materials [45]. The models based on damage accumulation are based on calculations of the field of a distribution of dislocations, as in the model by Weertman [46], or on a calculation of the energy balance necessary for crack advance, as in the model by Rice [47]. The particularities related to the very small grain sizes and large fraction of grain boundaries of the nanocrystalline materials discussed above are not taken into account. The very small grain sizes also promote a more homogeneous distribution of the damage, as discussed by Misra and co-workers [48].

4. Summary and future directions

In this paper, we reviewed the research, which is fairly recent, related to atomistic modeling of fatigue-crack growth in FCC metals at the nanoscale and have added some new simulation results to provide understanding of nanostructurally small cracks (NSC). In single crystals, fatigue damage was caused by persistent slip band formation, and crack growth was simulated using center crack specimens. The crack tip plasticity formation determined by the number of active slip systems was the main influencing factor for the propagation of nanocracks. The crystallographic orientation played an essential role in determining the particular type of dislocation structure experienced in single crystals. For orientations resulting in double slip at the crack tip, the plasticity localized in the two active slip bands leading to significant crack tip blunting. In such a situation, the crack propagated along one of the slip bands, leading to a mixed Mode I + II crack growth. For orientations resulting in multiple slip systems concomitantly active at the crack tip, the plastic deformation was distributed more evenly around the crack tip similar to isotropic hardening, yielding a diffuse isotropic plastic zone. In general, the propagation mechanism for nanocracks included void nucleation in front of the crack tip with a high density of dislocations and then the void linked back to the main crack to incur crack growth. In other situations, crack propagation involved only cleavage of atomic bonds in the crack plane leading to crack extension.

The molecular dynamics simulations revealed that NSC growth rates based upon the CTOD were found to be comparable with those of microstructural cracks, but significantly greater than those of long cracks. In addition, nanoscale cracks were found to grow at stress-intensity-factor ranges well below the commonly accepted values for long cracks. This indicates that improved multiscale theories of fatigue damage progression in metals, cannot neglect these accelerated crack growth rates for cracks in the nanometer range.

Analysis of crack growth at grain boundaries revealed that for high misorientation angles, the crack path deviated at the grain boundary. For high misorientation angles between the active (1 1 1) planes, grain boundaries acted as barriers, which trapped dislocations. For no misorientation of the active (1 1 1) planes in the two grains, the dislocations easily crossed the grain boundary. In this case, the grain boundary became almost indistinctive from the surrounding grains with the prevalent features being dislocation structures. The atomistic simulations revealed the formation

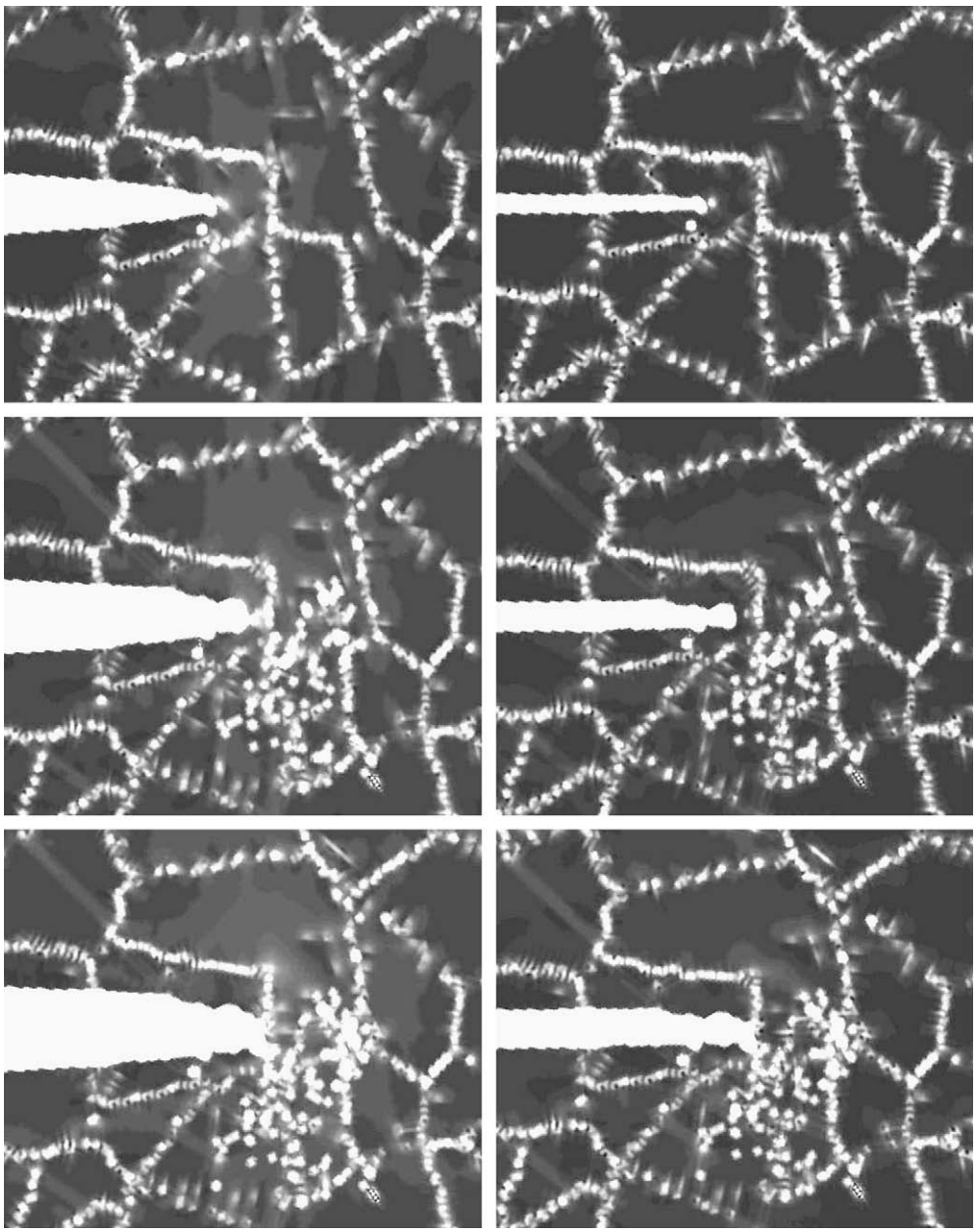

Fig. 38. Crack tip configurations for cycles 1, 12, and 20 for nanocrystalline nickel. Molecular statics with $\Delta K = 1.28$ MPa $\sqrt{}$m. Left frames are for maximum loading and right frames for minimum loading.

of different dislocation structures, such as slip bands and vein structures, based on the crystallographic orientation. In addition, vacancy formation was observed during the fatigue simulations. Due to the different stress regions created at the crack tip and the intergranular constraint between the two adjacent grains, we observed the formation of dislocation cells and walls. The atomistic simulations also clearly revealed that, according to different tilt angles of the grain boundaries, different slip systems could be activated at the same time. In general, the nanocrack followed the slip band path with the highest resolved shear stress. In the vicinity of the grain boundary, the crack growth mechanism was governed by the void nucleation and slip band formation.

The first atomistic studies of fatigue behavior in Ni nanocrystalline materials showed a Paris Law exponent of two, and a mechanism that was dominated by the role of the dislocations emitted from the crack tip, with a crack advance that blunted because of the emitted dislocations. Our results are consistent with experimental measurements of crack advance rates [30]. Furthermore, the nanovoids found ahead of the crack tip are in agreement with simulations and experimental transmission electron microscopy results obtained for monotonic fracture [38].

Clearly, MD and MS fatigue simulations have recently been used to reveal mechanisms at the nanoscale but for greater impact several new research endeavors are warranted:

1. To date, only FCC metals have been investigated. BCC and HCP materials need to be examined since many structural materials such as iron, steel, magnesium, titanium might find their way into nanostructural materials.
2. Because of the "welding" that occurs in the $R = -1$ simulations, an increasing applied load was used to characterize the nanoscale crack growth. Clearly, different R-values and boundary

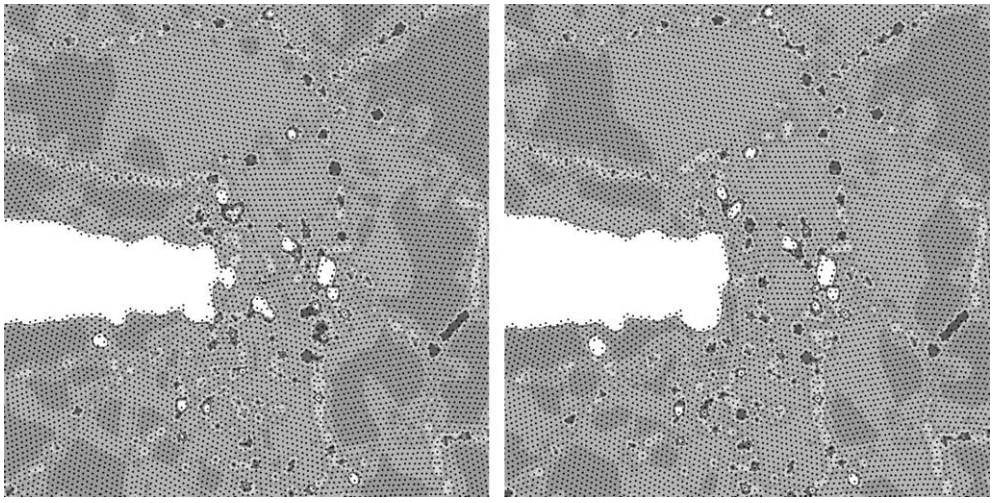

Fig. 39. Crack tip configurations for 26 (left) and 31 (right) cycles for nanocrystalline nickel. Molecular statics with $\Delta K = 1.28$ MPa $\sqrt{m}$. Frames show maximum loading.

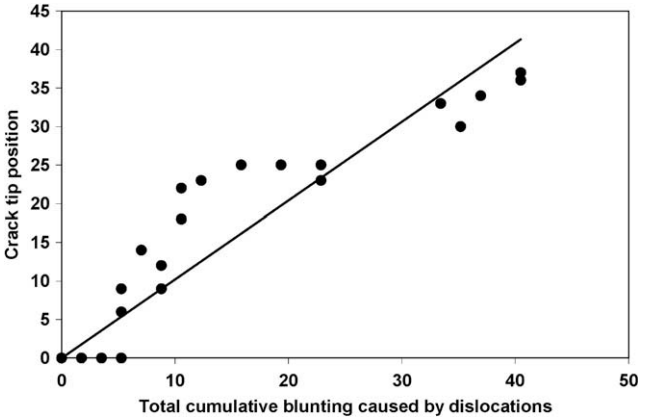

Fig. 40. Crack tip position plotted as a function of the total cumulative blunting caused by dislocation emission for nanocrystalline nickel.

conditions for that matter are needed to examine the different stress state effects that could be observed in nanostructural materials.

3. Temperature dependent nanoscale cyclic plasticity and fatigue has yet to be studied. MD and MC could be used to quantify the temperature effects at different applied strain rates (frequencies).
4. The bridge between atomistic scale fatigue and dislocation density fatigue simulations needs to be defined and used for multiscale materials modeling. This in turn, could motivate the development of microstructurally small crack modeling efforts from a physical basis.
5. Quantifying high cycle fatigue is an issue currently with MS, MD, and/or MC methods so garnering larger time periods would be of research interest.
6. Methods to get more realistic boundary conditions from higher scale conditions are warranted in order to get quantitatively more precise crack growth values. Currently, we can get several dislocations in these molecular dynamics simulations, and sometimes the small length of the specimens admits more dislocations where larger scale grains would not otherwise induce.
7. Because strain levels of 0.01 are required to grow a crack in MD with only one local defect (void or crack), one might speculate that in engineering materials, where many defects are present, lower strains can induce the crack growth because of the many defects.
8. Including molecular dynamics studies with probabilistic distributions of microstructures and grain boundaries that lead to macroscale fatigue predictive tools can also be a fruitful endeavor. The single crystal, simple bicrystal, and simple polycrystalline studies conducted to date provide only a starting point for NSC behavior.

Acknowledgements

MFH, TT, and SK would like to acknowledge the Center for Advanced Vehicular Systems (CAVS) at Mississippi State University for supporting this work.

References

[1] Vinogradov, Hashimoto S. Multiscale phenomena in fatigue of ultra fine grain materials: an overview: special issue on the progress in understanding of materials fracture. Mater Trans JIM 2001;42:74–84.
[2] Sih GC. Modeling of multiscale fatigue crack growth: nano/micro and micro/macro transitions, virtual testing and predictive modeling. Springer; 2009. p. 187–219.
[3] Fish J, Yu Q. Computational mechanics of fatigue and life predictions for composite materials and structures. Comput Method Appl Mech Eng 2002;191:4827–49.
[4] Van KD. Introduction to fatigue analysis in mechanical design by the multiscale approach. Springer-Verlag; 1999.
[5] Oskay C, Fish J. Modeling of fatigue of ductile materials. Int. J. Comp. Multiscale Eng 2004.
[6] Potirniche GP, Horstemeyer MF, Jelinek B, Wanger GJ. Fatigue damage in nickel and copper single crystals at nanoscale. Int J Fatigue 2005;27:1179–85.
[7] Potirniche GP, Horstemeyer MF. On the growth of nanoscale fatigue cracks. Philos Mag Lett 2006;86:185–93.
[8] Potirniche GP, Horstemeyer MF, Gullett PM, Jelinek B. Atomistic modeling of fatigue crack growth and dislocation structuring in FCC crystals. Proc Roy Soc A, London 2006;462:3707–31.
[9] Farkas D, Willemann M, Hyde B. Atomistic mechanisms of fatigue in nanocrystalline metals. Phys Rev Lett 2005;94:165–502.
[10] Yang Y, Imasogie B, Fan GJ, Liaw PK, Soboyejo WO. Fatigue and fracture of a bulk nanocrystalline nife alloy. Metall Mater Trans A 2008;39A:1145–56.
[11] Nishimura K, Miyazaki N. Molecular dynamics simulation of crack growth under cyclic loading. Comput Mater Sci 2004;31:269–78.
[12] Chang Win-Jin, Fang Te-Hua. Influence of temperature on tensile and fatigue behavior of nanoscale copper using molecular dynamics simulation. J Phys Chem Solids 2003;64:1279–83.
[13] Daw MS, Baskes MI. Semiempirical, quantum, mechanical calculation of hydrogen embrittlement in metals. Phys Rev Lett 1983;50:1285–8.
[14] Daw MS, Foiles SM, Baskes MI. The embedded-atom method: a review of theory and applications. Mater Sci Rep 1993;9:251–310.
[15] Baskes MI. Modified embedded-atom potentials for cubic materials and impurities. Phys Rev B 1992;46:2727–33.

[16] Baskes MI. Determination of modified embedded atom method parameters for nickel. Mater Chem Phys 1997;50:152–8.
[17] Mishin Y, Farkas D. Interatomic potentials for monoatomic metals from experimental data and ab initio calculations. Phys Rev B 1999;59:3393–407.
[18] Farkas D, Van Swygenhoven H, Derlet PM. Intergranular fracture in nanocrystalline metals. Phys Rev B 2002;66:101–4.
[19] Mendelev MI, Kramer MJ, Ott RT, Sordelet DJ, Yagodin D, Popel P. Development of suitable interatomic potentials for simulation of liquid and amorphous Cu–Zr alloys. Philos Mag 2009;89:967–87.
[20] Li C. On the interaction among Stage 1 short crack, slip band and grain boundary: a FEM analysis. Int J Fract 1990;43:227–39.
[21] Van Swygenhoven H, Farkas D, Caro A. Grain-boundary structures in polycrystalline metals at the nanoscale. Phys Rev B 2000;62:831–8.
[22] Kelchner CL, Plimpton SJ, Hamilton JC. Dislocation nucleation and defect structure during surface indentation. Phys Rev B 1998;58:11085–8.
[23] Laird C. The influence of metallurgical structure on the mechanisms of fatigue crack propagation fatigue crack propagation. ASTM STP Am Soc Test Mater 1967;415:131.
[24] Miller KJ. The behavior of short fatigue cracks and their initiation part I – a review of two recent books. Fatigue Fract Eng Mater Struct 1987;10:75–91.
[25] Miller KJ. The behavior of short fatigue cracks and their initiation part ii – a general summary. Fatigue Fract Eng Mater Struct 1987;10:93–113.
[26] Zurek K, James MR, Morris WL. The effect of grain size on fatigue growth of short cracks. Metal Mater Trans 1982;14A:1697–705.
[27] Buque C. Dislocation structures and cyclic behavior of [0 1 1] and [11-1]-oriented nickel single crystals. Int J Fatigue 2001;23:671–8.
[28] Zhang ZF, Wang ZG, Sun ZM. Evolution and microstructural characteristics of deformation bands in fatigued copper single crystals. Acta Mater 2001;102:2875–86.
[29] Marchand NJ, Bailon J-P, Dickson JI. Near-threshold fatigue crack growth in copper and alpha-brass: grain-size and environmental effects. Metal Trans A 1988;19A:2575–87.
[30] Liaw PK, Leax TR, Logsdon A. Near-threshold fatigue crack growth behavior in metals. Acta Metal 1983;31:1581–7.
[31] Wang R, Mughrabi H. Fatigue of copper single crystals in vacuum and in air, II: fatigue crack propagation. Mater Sci Eng 1984;65:235–43.
[32] Pol'ak J, Lĭskufın. Nucleation and short crack growth in fatigued polycrystalline copper. Fatigue Fract Eng Mater Struct 1990;13:119–33.
[33] Paris PC, Erdogan F. A critical analysis of crack propagation laws. J Basic Eng 1960;85:528–34.
[34] Potirniche GP, Daniewicz SR. Analysis of crack tip plasticity for microstructurally small cracks using crystal plasticity theory. Eng Fract Mech 2003;70:1623–43.
[35] Fan J, McDowell DL, Horstemeyer MF, Gall KA. Computational micromechanics analysis of cyclic crack tip behavior for microstructurally small cracks in dual-phase Al–Si alloys. Eng Fract Mech 2001;68:1687–706.
[36] Li C. On crystallographic crack transfer across interfaces in four types of aluminum bicrystal. Mater Sci Eng A 1994;183:23–30.
[37] Hanlon T, Kwon YN, Suresh S. Grain size effects on the fatigue response of nanocrystalline metals. Scripta Mater 2003;49:675680.
[38] Suresh S. Fatigue of materials. second ed. Cambridge (England): Cambridge University Press; 1998.
[39] Weertman J. Dislocation based fracture mechanics. first ed. Singapore: World Scientific Publishing; 1996.
[40] Weertman J. In: Soboyejo WO, Srivatsan TS, editors. High cycle fatigue of structural materials. Warrendale (PA): The Minerals, Metals and Materials Society (TMS) of the AIME; 1997. p. 1–48.
[41] Deshpande VS, Needleman A, Van der Giessen E. Discrete dislocation modeling of fatigue crack propagation. Acta Mater 2002;50:831–46.
[42] Deshpande VS, Needleman A, Van der Giessen E. Discrete dislocation plasticity modeling of short cracks in single crystals. Acta Mater 2003;51:1–15.
[43] Deshpande VS, Needleman A, Van der Giessen E. Scaling of discrete dislocation predictions for near-threshold fatigue crack growth. Acta Mater 2003;51:4637–51.
[44] Deshpande VS, Needleman A, Van der Giessen E. A discrete dislocation analysis of near-threshold fatigue crack growth. Acta Mater 2001;49:3189–203.
[45] Kumar KS, Van Swygenhoven H, Suresh S. Mechanical behavior of nanocrystalline metals and alloys. Acta Mater 2003;51:5743–74.
[46] Weertman J. Int J Fract Mech 1966;2:460.
[47] Rice JR. Fatigue crack propagation, vol. 415. Philadelphia: ASTM; 1967. p. 247.
[48] Misra A, Kung H, Hammon D, Hoagland RG, Nastasi M. Damage mechanisms in nanolayered metallic composites. Int J Damage Mech 2003;12:365–76.
[49] Daw MS, Foiles SM, Baskes MI. The embedded-atom method: a review of theory and applications. Mater Sci Rep, A Rev J 1993;9(7–8):251–310.
[50] Horstemeyer MF, Baskes MI. Atomistic finite deformation simulations: a discussion on length scale effects in relation to mechanical stresses. J Eng Mater Tech Trans ASME 1999;121:114–9.
[51] Horstemeyer MF, Baskes MI, Hughes DA, Godfrey A. Orientation effects on the stress state of molecular dynamics large deformation simulations. Int J Plast 2002;18:203–9.
[52] Horstemeyer MF, Plimpton SJ, Baskes MI. Size scale and strain rate effects on yield and plasticity of metals. Acta Mater 2001;49:4363–74.
[53] Horstemeyer MF, Baskes MI, Plimpton SJ. Computational nanoscale plasticity simulations using embedded atom potentials. In: George Sih, editor. Prospects in mesomechanics. Theor Appl Fract Mech, 2001;37(1–3):49–98.
[54] Brenner DW. Chemical dynamics and bond-order potentials. MRS Bull 1996:36–41.
[55] Stoneham M, Harding J, Harker T. The shell model and interatomic potentials for ceramics. MRS Bull 1996:29–35.
[56] Hansen N, Hughes DA. Analysis of large dislocation populations in deformed metals. Phys Stat Solid: B 1995;149:155–72.
[57] Baskes MI, Angelo JE, Bison CL. Atomistic calculations of composite interfaces. Model Simulat Mater Sci Eng 1994;2:505–18.
[58] Gall KA, Horstemeyer MF, Van Schilfgaarde M, Baskes MI. Atomistic simulations on the tensile debonding of an aluminum–silicon interface. J Mech Phys Solids 2000;48:2183–212.
[59] Fang H, Horstemeyer MF, Baskes MI, Solanki K. Atomistic simulations of Bauschinger effects of metals with high angle and low angle grain boundaries. Comput Methods Appl Mech Eng 2004;193:1789–802.
[60] Gullett PM, Horstemeyer MF, Baskes MI, Fang H. Deformation gradient tensor and strain tensors for atomistic simulations. MSMSE 2008;6:1–17.
[61] McDowell DL, Gall K, Horstemeyer MF, Fan J. Microstructure-based fatigue modeling of cast A356-T6 alloy. Eng Fract Mech 2003;70:49–80.
[62] Deng C, Sansoz F. Fundamental differences in the plasticity of periodically twinned nanowires in Au, Ag, Al, Cu, Pb and Ni. Acta Mater 2009;57(20):6090–101.
[63] Sansoz F, Molinari JF. Size and microstructure effects on the mechanical behavior of FCC bicrystals by quasicontinuum method. Thin Solid Films 2007;515(6):3158–63.
[64] Warner DH, Curtin WA. Origins and implications of temperature-dependent activation energy barriers for dislocation nucleation in face-centered cubic metals. Acta Mater 2009;57(14):4267–77.
[65] Rittner JD, Seidman DN. Limitations of the structural unit model. Mater Sci Forum 1996;207–209(1):333–6.
[66] Tschopp MA, McDowell DL. Structures and energies of $\sum 3$ asymmetric tilt grain boundaries in copper and aluminium. Philos Mag 2007;87(22):3147–73.
[67] Tschopp MA, McDowell DL. Asymmetric tilt grain boundary structure and energy in copper and aluminium. Philos Mag 2007;87(25):3871–92.
[68] Olmsted David L, Holm Elizabeth A. Survey of computed grain boundary properties in face-centered cubic metals-II: grain boundary mobility foiles. In: Stephen M, editor. Acta Mater, 2009;57(13):3704–13.
[69] Olmsted David L, Foiles Stephen M, Holm Elizabeth A. Survey of computed grain boundary properties in face-centered cubic metals: I. Grain boundary energy. Acta Mater 2009;57(13):3694–703.
[70] Zhou Lang, Zhang Hao, Srolovitz David JA. Size effect in grain boundary migration: a molecular dynamics study of bicrystal thin films. Acta Mater 2005;53(20):5273–9.
[71] Kim Ki Jung, Yoon Jang Hyuk, Cho Min Hyung, Jang Ho. Molecular dynamics simulation of dislocation behavior during nanoindentation on a bicrystal with a $\Sigma = 5(210)$ grain boundary. Mater Lett 2006;60(28):3367–72.
[72] Wang L, Zhang HW, Deng X. Influence of defects on mechanical properties of bicrystal copper grain boundary interfaces. J Phys D: Appl Phys 2008;41(13).
[73] Luque A, Aldazabal J, Martínez-Esnaola JM, Gil Sevillano J. Molecular dynamics simulation of crack tip blunting in opposing directions along a symmetrical tilt grain boundary of copper bicrystal. Fatigue Fract Eng Mater Struct 2007;30(11):1008–15.
[74] Spearot Douglas E, Jacob Karl I, McDowell David L. Dislocation nucleation from bicrystal interfaces with dissociated structure. Int J Plast 2007;23(1):143–60.
[75] Spearot Douglas E, Jacob Karl I, McDowell David L, Plimpton Steven J. Effect of deformation path sequence on the behavior of nanoscale copper bicrystal interfaces. J Eng Mater Technol, Trans ASME 2005;127(4):374–82.
[76] Li Xiaofan, Hu Wangyu, Xiao Shifang, Huang Wei-Qing. Molecular dynamics simulation of polycrystalline molybdenum nanowires under uniaxial tensile strain: size effects. Phys E: Low Dimens Syst Nanostruct 2008;40(10):3030–6.
[77] Zahn Dirk. Molecular dynamics simulation of optimized shearing routes in single- and polycrystalline aluminum. Comput Mater Sci 2009;45(4):845–8.
[78] Shabib Ishraq, Miller Ronald E. Deformation characteristics and stress–strain response of nanotwinned copper via molecular dynamics simulation. Acta Mater 2009;57(15):4364–73.
[79] Zhang D-B, Hua M, Dumitric T. Stability of polycrystalline and wurtzite Si nanowires via symmetry-adapted tight-binding objective molecular dynamics. J Chem Phys 2008;128(8).
[80] Krivtsov Anton M. Molecular dynamics simulation of impact fracture in polycrystalline materials. Meccanica 2003;38(1):61–70.
[81] Holian Brad Lee, Abraham Farid F, Ravelo Ramon. Fracture simulations via massively parallel molecular dynamics. Adv Comput Methods Mater Model 1993;180:207–17.
[82] Abraham Farid F, Brodbeck Dominique, Rudge William E, Xu Xiaopeng. Molecular dynamics investigation of rapid fracture mechanics. J Mech Phys Solids 1997;45(9):1595–619.